12-2016

The Kinematics and X-ray Emission Mechanism of the Large-Scale Jet of 3C 111

Devon Clautice

The Kinematics and X-ray Emission Mechanism of the Large-Scale Jet of 3C 111

by

Devon Clautice

Bachelor of Science
Physics and Mathematics
University of Central Florida
2010

A thesis submitted to Florida Institute of Technology
in partial fulfillment of the requirements
for the degree of

Master of Science
in
Space Sciences

Melbourne, Florida
December 2016

We the undersigned committee hereby recommends that the attached document be accepted as fulfilling in part of the requirements for the degree of Master of Science of Space Sciences

"The Kinematics and X-ray Emission Mechanism of the Large-Scale Jet of 3C 111"
a thesis by
Devon Clautice

Eric Perlman, Ph.D.
Professor, Physics and Space Sciences
Major Advisor

Véronique Petit, Ph.D.
Assistant Professor, Physics and Space Sciences
Committee Member

Joel Olson, Ph.D.
Associate Professor, Chemistry
External Committee Member

Daniel Batcheldor, Ph.D.
Interim Department Head, Physics and Space Sciences

Abstract

The Kinematics and X-ray Emission Mechanism of the Large-Scale Jet of 3C 111

by Devon Clautice

Thesis Advisor: Eric Perlman, Ph.D.

Relativistic jets are the most energetic manifestation of the active galactic nucleus (AGN) phenomenon. AGN jets are observed from the radio through gamma rays and carry copious amounts of matter and energy from the sub-parsec central regions out to the kiloparsec and often megaparsec scale galaxy and cluster environs. While most spatially-resolved jets are seen in the radio, an increasing number have been discovered to emit in the optical/near-IR and/or X-ray bands. Here we discuss a spectacular example of this class, the 3C 111 jet, housed in one of the nearest, double-lobed FR II radio galaxies known. We discuss new, deep *Chandra* and *HST* observations that reveal both near-IR and X-ray emission from several components of the 3C 111 jet, as well as both the approaching and receding hotspots. Important morphological differences are seen between the radio, X-ray, and near-IR bands. The long (over 100 kpc), straight nature of this jet makes it an excellent prototype for future, deep observations, as it is one of the longest such features seen in the radio, near-IR/optical, and X-ray bands. It is also just the sixth case where both jet lobes have been detected in the X-rays. Several independent lines of evidence, including the X-ray and broadband spectral shape as well as the implied velocity of the approaching hotspot, lead us to strongly disfavor the EC/CMB model and instead favor a two-component synchrotron model to explain the observed X-ray emission for several jet components. Additional future observations with *HST*, *Chandra*, and *NuSTAR* will allow us to greatly expand on the current analyses and constrain the emission mechanisms for many of the faint jet knots.

Contents

List of Figures

List of Tables

Abbreviations

ACIS	**A**dvanced **C**CD **I**maging **S**pectrometer
AGN	**A**ctive **G**alactic **N**ucleus/**N**uclei
AIPS	**A**stronomical **I**mage **P**rocessing **S**ystem
CASA	**C**ommon **A**stronomy **S**oftware **A**pplications
CCD	**C**harge **C**oupled **D**evice
CIAO	**C**handra **I**nteractive **A**nalysis of **O**bservations
CTE	**C**harge **T**ransfer **E**fficiency
DN	**D**ata **N**umber
EC/CMB	**E**xternal inverse-**C**ompton Scattering of the **C**osmic **M**icrowave **B**ackground
FITS	**F**lexible **I**mage **T**ransport **S**ystem
FR I/II	**F**anaroff-**R**iley Class **I/II**
HETG	**H**igh **E**nergy **T**ransmission **G**rating
HST	**H**ubble **S**pace **T**elescope
IRAF	**I**mage **R**eduction and **A**nalysis **F**acility
LETG	**L**ow **E**nergy **T**ransmission **G**rating
NHS	**N**orthern **H**ot**s**pot
NICMOS	**N**ear **I**nfrared **C**amera and **M**ulti-**O**bject **S**pectrometer
NuSTAR	**Nu**clear **S**pectroscopic **T**elescope **Ar**ray
PSF	**P**oint **S**pread **F**unction
SED	**S**pectral **E**nergy **D**istribution
SHS	**S**outhern **H**ot**s**pot
SSC	**S**ynchrotron **S**elf-**C**ompton
VLA	**V**ery **L**arge **A**rray
VLBI	**V**ery **L**ong **B**aseline **I**nterferometry
WCS	**W**orld **C**oordinate **S**ystem
WFC3	**W**ide **F**ield **C**amera **3**
WFPC2	**W**ide **F**ield and **P**lanetary **C**amera **2**

Acknowledgements

I wish to thank my parents, Russ and Gloria Clautice, without whom this would not be possible. I wish also to thank Dr. Eric Perlman for being my advisor. And lastly, I wish to thank my friends for their help and support.

These results are based on observations made by the *Chandra* X-ray Observatory and *Hubble Space Telescope*, as well as the Very Large Array (*VLA*). We acknowledge support for this work by the National Aeronautics and Space Administration (NASA) through Chandra award G03-14113A issued by the Chandra X-ray Observatory Center, which is operated by the Smithsonian Astronomical Observatory for and on behalf of the National Aeronautics and Space Administration under contract NAS8-03060. We also acknowledge support from HST grant GO-13114.01, which was provided by NASA through a grant from the Space Telescope Science Institute, which is operated by the Association of Universities for Research in Astronomy, Inc., under NASA contract NAS 5-26555. The National Radio Astronomy Observatory is a facility of the National Science Foundation operated under cooperative agreement by Associated Universities, Inc.

I dedicate this thesis to my best friend Tom Schaer, whose arrogance is matched only by his rudeness.

Chapter 1

Introduction

The work presented in this thesis has previously been published in The Astrophysical Journal (Clautice et al., 2016).

Active galactic nuclei (AGN) are small regions at the core of some galaxies that are characterized by extremely high energy output. Nearly every galaxy is thought to have a supermassive black hole at its core − a black hole with mass on the order of millions or even billions of solar masses. At any time, the vast majority of these supermassive black holes are quiescent, however a small percentage ($\sim 1\%$) are able to accrete enough matter that they begin to outshine the stars and other sources of electromagnetic radiation in their galaxy. Of this small number of "active" galaxies, about 10% are seen to form relativistic jets (Kellermann et al., 1989) − very powerful and highly-collimated outflows that emit electromagnetic radiation over a wide range of wavelengths, from radio through gamma rays.

This thesis will focus on a multiwavelength study of the jet of 3C 111, including recent near-infrared observations from the *Hubble Space Telescope* (*HST*) using the new Wide Field Camera 3 (WFC3) as well as an older observation using the now-replaced Wide Field Planetary Camera 2 (WFPC2); recent observations in the X-ray regime

using the *Chandra X-Ray Observatory* (*Chandra*), and archival radio observations from the Very Large Array (VLA). Our main goal is to determine the emission mechanism that is primarily responsible for the observed X-ray flux.

Modified portions of this thesis have previously been published in Clautice et al. (2016). This includes the abstract and much of the work presented in §3.1 and Chapters 4 and 5.

1.1 Relativistic Jets

The first observation of an AGN jet was from the galaxy M87 in 1918 using an early radio telescope. Over the following decades and thanks to improvements in telescope technology, radio jets were detected in more and more galaxies. These jets are thought to be propelled by the supermassive black hole in a way that is not well-understood (discussed in §1.3). Whatever the exact mechanism, the jets are propelled at tremendous speeds (nearly the speed of light, c) outward from the core and are able to carry energy and momentum out to distances of a megaparsec or more. These sources are among the most energetic phenomena in the Universe, with a typical jet radiative power of $10^{42} - 10^{47}$ erg s^{-1}.

Early ground-based optical observations were able to detect optical emission in a handful of these jets, but it was not until *HST* came online in 1990 that the true extent of optical jet emission was first seen. Once *Chandra* was launched in 1999, jet emission was detected in the X-ray band, which was not expected. *Chandra*'s first calibration observation was of the quasar PKS 0637-752, which turned out to have an obvious jet flowing from its core (Schwartz et al., 2000). *Chandra* has allowed for easier detection of optical jets, as well, since optical knots can be difficult to detect without knowing they are there due to the presence of many background sources. To date, at least 117 X-ray

jets have been identified[1] while ∼45 jets have confirmed optical emission (Boettcher et al., 2012, p. 155). Lister & Marscher (1997) estimate that there must be a parent population of $\gtrsim$10 million jets in the observable Universe, though due to relativistic effects (discussed in §1.5) only 293 have been detected in radio surveys (Taylor et al., 1996).

AGN jets can be broken down into categories based on observational differences. One such classification is the Fanaroff-Riley (FR) scheme − FR I and FR II (Fanaroff & Riley, 1974). FR I jets are less powerful than FR II jets, with the division happening at $L_{1.4\ \mathrm{GHz}} \sim 5 \times 10^{25}$ W Hz^{-1}, and have several distinctions that will be highlighted in §1.4. Depending on their orientation and bulk velocity, either one or both of the approaching and receding jets will be seen.

1.2 Disk Accretion

Nearly every galaxy is thought to have a supermassive black hole at its core. The process by which matter falls into such a black hole is known as accretion. The matter supply can come from either the interstellar medium (ISM) or from stars that become tidally disrupted near the black hole. Infalling matter will have a nonzero angular momentum; the centrifugal force caused by the rotation around the black hole causes the matter to form into a disk or torus structure (Figure 1.1).

To continue falling in, the matter in the accretion disk must somehow lose some of its angular momentum. Theoretically, friction caused by the molecular viscosity of the accreting "fluid" can allow for angular momentum to be transferred outward along the disk, allowing matter on the interior of the disk to fall further in. However, this friction is too small to be the main mechanism of angular momentum transfer in the disk. It was

[1] `http://hea-www.harvard.edu/XJET/`

postulated by Shakura & Sunyaev (1973) that a source of hydrodynamic turbulence could be responsible for increasing the viscosity of the fluid, thereby increasing the angular momentum transfer and allowing matter in the inner accretion disk to continue falling into the black hole. Balbus & Hawley (1991) showed that the presence of even a very weak magnetic field can induce such a turbulence, leading to an instability in the disk. This effect is known as the magnetorotational instability (MRI) and is thought to be important in many astrophysical systems.

The nature of the magnetic fields present in accretion disks is still an open question, though it is largely agreed that they play an important role. It is possible that such disks exhibit a dynamo effect that generates its own magnetic field, or that the magnetic field present in the ISM is dragged along with the infalling matter as it spirals into a disk.

An accretion disk can be either "thin" or "thick" depending on how efficiently the disk matter is being cooled. If the radiative cooling of the plasma is very efficient, the disk will be geometrically thin; otherwise, it will be thick or torus-shaped. In general, a higher mass accretion rate leads to an increase in disk thickness. The Eddington luminosity (or Eddington limit) is the theoretical maximum luminosity possible, when the gravitational force inward is equal to the radiation pressure outward; this occurs at the corresponding Eddington (mass) accretion rate. When the mass accretion rate exceeds this critical value, the radiation pressure increases above the Eddington limit (becoming so-called super-Eddington). The increased radiation pressure serves to overpower the inward gravitational force and has a net effect of slowing the rate of accretion. This self-regulating process serves to keep the mass accretion rate at roughly the Eddington rate except for short durations.

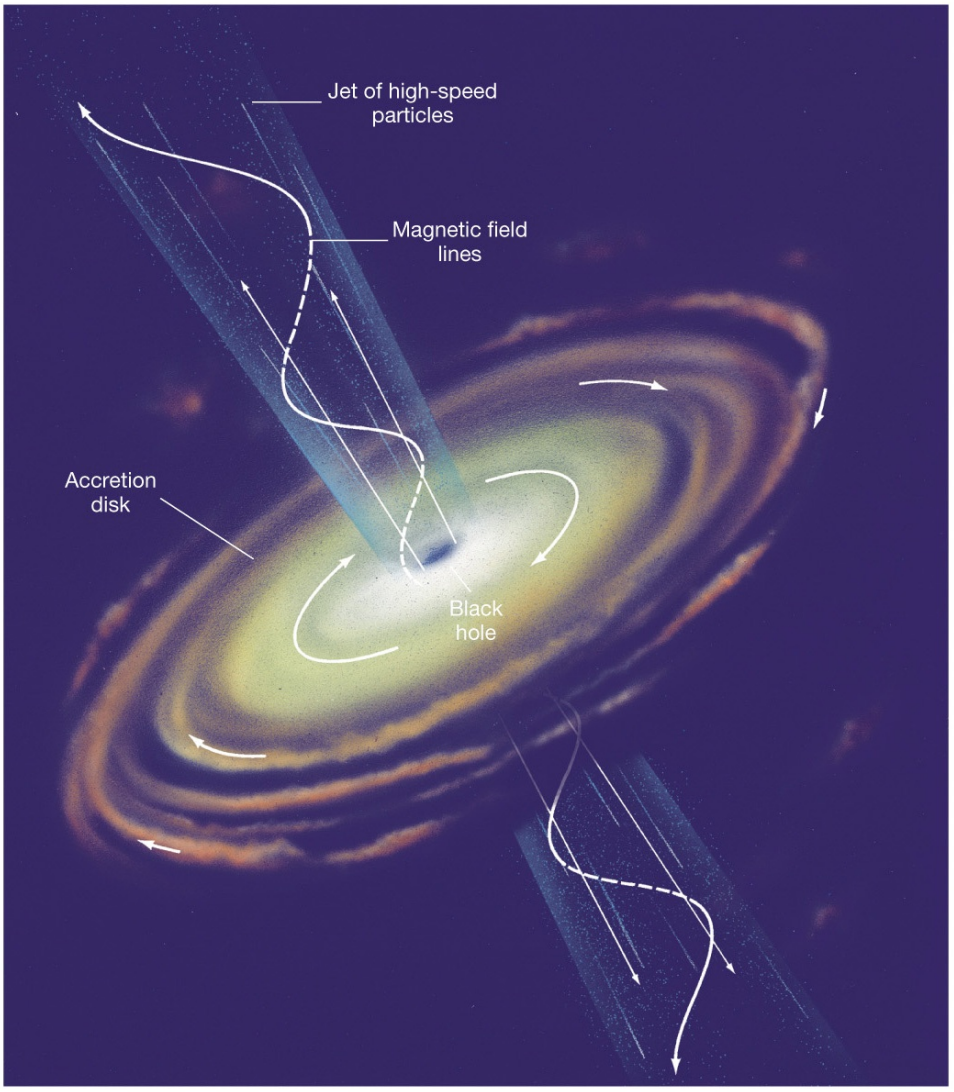

Figure 1.1 Illustration of an AGN that is launching a relativistic jet. Credit: Pearson Education, Inc.

The fraction of jetted AGN has been observed to increase with cosmological redshift (e.g., Jiang et al. 2007). This is thought to be due to the nature of the black-hole-accretion-disk systems that are capable of launching jets, though the possibilities are largely speculative. One such possibility is that a spinning (Kerr) black hole is required to launch a jet, and that the spin must be close to maximal (e.g., Meier 1999). Prograde accretion can increase the spin of a black hole to its maximum in a timescale of

$\sim M/\dot{M}$ (Tout & Pringle, 1996), while retrograde accretion decreases black hole spin on an even shorter timescale (Moderski et al., 1998). Given that accretion can randomly be prograde or retrograde, this would lead to an overall effect where, over time, most black holes become slow rotators and incapable of launching jets. Black hole mergers (likely during galactic mergers) could also spin up the black hole, and such mergers are thought to be much more common in the early Universe.

Another intriguing possibility is that jets can only be launched from retrograde accretion disk systems (Wilson & Colbert, 1995). Accretion disk systems are thought to have a "plunging region" where material that falls within the last stable circular orbit will quickly fall into the accreting black hole. Depending on the density of matter in this plunging region at any given time, a large magnetic flux can accumulate. This effect is thought to be strongest for a retrograde disk, and would give such a disk the strongest possible magnetic flux with which to launch a jet (discussed further in §1.3). Over time, retrograde disk accretion will spin down its black hole until it becomes prograde. This could explain the rarity of jetted AGN, requiring a rare event such as a galactic merger to cause retrograde accretion on a prograde supermassive black hole system. This model is supported by the observation of several supermassive black holes exhibiting rapid prograde spin but no jets (e.g., Brenneman & Reynolds 2006).

These examples serve to demonstrate a common fact of studying jets − there are many possible models that have been found to explain any given aspect of jet physics, however there are currently few observational methods with which to constrain which models are actually at work.

1.3 Jet Formation

It is thought that the supermassive black hole and its associated accretion disk are responsible for accelerating a jet outward from the core. Very Long Baseline Interferometry (VLBI) observations of M87 have traced the jet to very near the black hole nucleus (Krichbaum et al., 2006). The gravitational potential energy of the infalling matter and the spinning black hole are the only obvious sources of power present that could serve as an engine for the jet. Also important are the strong magnetic fields produced by the accretion disk - rotating black holes cannot have their own magnetic fields. It is not known whether the accretion disk can generate its own magnetic field *in situ* via magnetic dynamo or whether gas from the ISM carries the magnetic fields as it accretes. The exact nature of jet launching is still an open question.

The two predominant models for relativistic jet launching are those of Blandford & Payne (1982) and Blandford & Znajek (1977). Both models rely on magnetic launching. The chief difference between them lies in the energy reservoir used to launch the jet.

The model of Blandford & Znajek (1977) relies on the extraction of energy and angular momentum from the black hole itself, with magnetic flux from the accretion disk being "squeezed" into the black hole's ergosphere. A Kerr black hole in the presence of a magnetic field will generate an electric field through general relativistic effects, allowing energy from the black hole to be extracted. In this model, it is primarily electrons and positrons (generated through pair production in the black hole's magnetosphere) which are launched initially, with protons being added from magnetic field lines that intersect the accretion disk or later on externally. The magnetic fields which are anchored in the accretion disk are rapidly rotating around to form a helical shape that serves to tightly collimate the jet (as in Figure 1.1). This is generally accepted to be the "easiest" (in terms of energy efficiency) method for a jet to be launched at ultrarelativistic speed. This model relies on the black hole magnetosphere to be "open" – open field lines

allowing for the transfer of angular momentum from the black hole to infinity – as opposed to "closed," where closed field lines can only transfer angular momentum to the accretion disk. "Open" magnetospheres are associated with both rapid prograde black holes and with retrograde black holes. For this mechanism, retrograde black holes are thought to launch the most powerful jets (e.g., Meier 2011).

The model of Blandford & Payne (1982) relies on the presence of magnetic field lines anchored in the disk that are being rapidly dragged to form a helical shape. Perturbations within the disk accelerate matter away from the disk and along the field lines (like beads on a string). The acceleration and collimation of the jet in this model is achieved by the magnetic field energy (Poynting flux) being converted into bulk kinetic energy and the presence of an external medium. This process is more efficient for non-relativistic jets than for relativistic ones.

It is possible that both mechanisms work to launch jets that follow the spine-sheath model (discussed in §1.4), where the central spine is powered by the ergosphere and the outer sheath is ejected from the accretion disk (Xie et al., 2012).

1.4 Structure and Composition

Once the jet is accelerated away from the core, the first structure that is observed comes in the form of blobs of emitting plasma called "knots." Shocks and magnetic reconnection phenomena within the jet are thought to accelerate electrons to relativistic speeds, which then emit electromagnetic radiation in various wavelengths and produce the observed knots. It is these locally-accelerated electrons that produce the emission observed in the IR-optical wavelengths by way of synchrotron and inverse-Compton emission (see §1.6). Knots can be seen on the smallest and largest scales. On the pc

scale, a stationary recollimation shock can occur where the pressure of the external medium serves to collimate the jet.

FR I jets exhibit decreasing brightness at greater distances from the core, with the jet terminating in large plumes. An FR II jet terminates at a very bright region called a "hotspot" which is surrounded by a large radio lobe. As the jet pushes through the much slower intergalactic medium (IGM), shocks form which accelerate electrons to relativistic speeds and create a bright hotspot; material is pushed away in the collision which form the lobes. Recent work using relativistic magnetohydrodynamic (MHD) simulations point to a kink instability being responsible for the FR dichotomy (Tchekhovskoy & Bromberg, 2016). Jets above a certain critical power are able to stably push through the ISM in the galaxy's core and terminate at hotspots (FR II), while jets below this critical power become unstable and lose their integrity, resulting in large plumes of hot plasma (FR I). Thus, they find it likely that the relation between the jet's power and the ISM density of the host galaxy dictates which type of jet it will be.

The composition of relativistic jets is largely unknown, though there are several constraints on what it must be. Firstly is the fact that jets extend over such massive scales, which rules out high-energy electrons as being the main source of energy transportation − such electrons would lose their energy long before reaching the hot spot (Harris & Krawczynski, 2007). In knots and hotspots, energy is transferred from the bulk composition of the jet into a population of the plasma; the emission that we observe from jets is due to the relativistic electrons that have been accelerated in these regions.

The possible candidates for the carrier of the bulk energy of the jet are thought to be: cold electrons/positrons, cold or hot protons, and Poynting flux (energy carried by electromagnetic fields) (e.g., Perucho & Martí 2007). While attempts have been made to determine which of these is dominant in jets, the ionized nature of the jet's

composition makes it difficult to determine − each attempt is fraught with assumptions and arguments that are contentious.

There is still a large gap in our understanding of how jets can remain highly collimated on the kpc scale. One popular explanation is the spine-sheath model, where a jet has two components: a central spine that is highly relativistic and an outer sheath that is moving slower. One would expect that such a jet would exhibit limb-brightening, where the emission from the fast-moving spine is de-boosted to a higher degree than the sheath emission (described in §1.5). Such limb-brightening has been observed in numerous jets (e.g., Giovannini et al. 1999). It is possible in such a model for observed radio emission to come from the sheath and X-ray emission to come from the spine, in which case a detected X-ray knot should be narrower than its associated radio knot; this has been seen in the nearby jet of M87 (Perlman & Wilson, 2005) and PKS 0637-752 (Celotti et al., 2001). A spine-sheath jet is thought to be stabilized from effects that would otherwise disrupt the collimation of the jet over large scales.

1.5 Relativistic Effects

AGN jets can have bulk Lorentz factors of $\Gamma > 10$ on the parsec scale (Lister et al., 2009) and can remain relativistic out to their kiloparsec-scale hotspots (Longair & Riley, 1979). Special relativity is thus important on both the small and large scales. On the parsec scale, this can cause jet knots to appear to move faster than the speed of light. On the large (kpc) scale, on which this project is focused, many relativistic effects are important.

1.5.1 Beaming and Boosting

Foremost is the effect of relativistic beaming. A region of the jet that is moving at relativistic speeds, assuming it emits photons isotropically in its rest frame, will have half of all the photons produced beamed into a narrow cone of opening angle $\theta = 1/\Gamma$ in the observer's reference frame (Figure 1.2). This has a large affect on the observed flux of the emitting region, making it very dependent on the angle between the jet's propagation and the observer's line of sight. For an approaching jet moving at speed v, this has the effect of increasing the observed flux and frequency of the photons. A receding jet is likewise de-boosted and less easy to detect. An emitted photon's energy will be boosted as

$$E^{\rm rec} = \delta E^{\rm em}, \tag{1.1}$$

where "rec" denotes the stationary observer's frame, "em" denotes the comoving frame of the emission region, and the Doppler factor is

$$\delta \equiv \frac{1}{\Gamma(1 - \beta_\Gamma \cos\theta)}. \tag{1.2}$$

Here, the bulk Lorentz factor $\Gamma = 1/\sqrt{1-\beta^2}$, $\beta_\Gamma = v/c$, and θ is the viewing angle – the angle between the jet and the line-of-sight of the observer in the observer's reference frame. Since the photon energy is related to its frequency by $E_{\rm ph} = h\nu$, it follows that the frequency is similarly boosted, such that $\nu^{\rm rec} = \delta\nu^{\rm em}$. Since the inverse of frequency is a time interval, it is also apparent that $\Delta t^{\rm rec} = \delta^{-1}\Delta t^{\rm em}$.

The effects of Doppler boosting compound when considering the flux. When comparing emission at $\nu^{\rm em}$ in the "em" frame and $\nu^{\rm rec}$ in the "rec" frame, the flux is boosted by a factor of δ^3, however when comparing the flux emitted at $\nu^{\rm rec}$ in both frames, we have

$$F^{\rm rec}_{\nu^{\rm rec}} = F^{\rm em}_{\nu^{\rm rec}}\delta^{3+\alpha}. \tag{1.3}$$

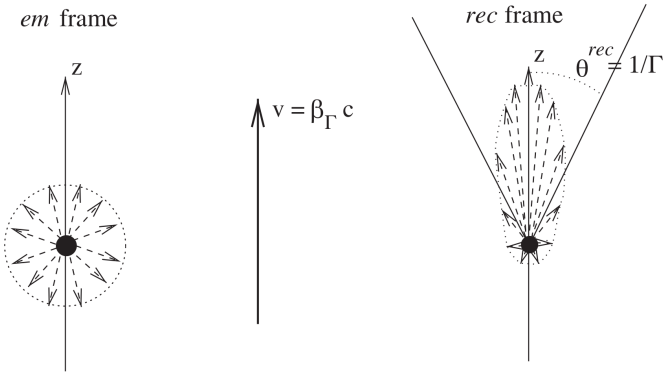

Figure 1.2 Light emitted isotropically in the comoving ("em") frame of the emission region is beamed in the direction of relativistic motion in the observer's ("rec") frame. From Boettcher et al. (2012).

This is well illustrated in Figure 1.3. Importantly, the effects of Doppler boosting do not alter the spectral index α of a power law ($F_\nu \propto \nu^{-\alpha}$). These effects, combined with others such as length contraction and time dilation, make it so that jet properties vary greatly with the viewing angle to the observer.

1.5.2 Superluminal Motion

Another peculiar effect of the relativistic motion of jets is the appearance, in some cases, of superluminal motion − that the proper motion of jet material is faster than the speed of light. Very high-resolution radio observations (e.g., VLBI) on the parsec scale allow for the tracking of jet knots over time. These knots can sometimes be moving with apparent speeds as high as $\beta_{\perp,app} \sim 50$ (Lister et al., 2009). This is due to the fact that we observe the projection of a jet onto the 2D plane of the sky (Rees, 1966). This effect is important because it allows one to constrain both the bulk Lorentz factor of the jet and the viewing angle.

In practice, it is the parameter μ, typically in units of milliarcseconds (mas) per year, that is measured directly from the proper motion of a parsec-scale jet component.

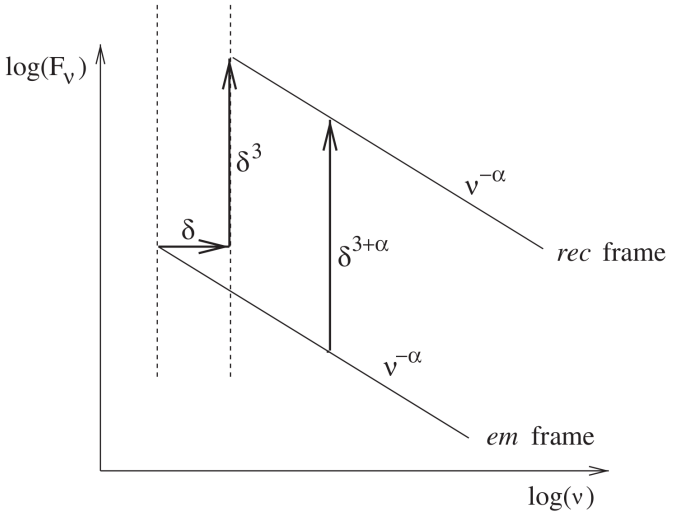

Figure 1.3 Illustration of the effects of relativistic Doppler boosting on a power law spectrum. From Boettcher et al. (2012).

From this, the apparent speed of the component $\beta_{\perp,\mathrm{app}}$ can be found by knowing the angular size distance $D_\mathrm{A} = D_\mathrm{L}/(1+z)^2$, where D_L is the luminosity distance[2] to the AGN and z is its cosmological redshift, such that $\beta_{\perp,\mathrm{app}} = \mu D_\mathrm{A}/c$. The redshift (and therefore the luminosity distance) of an AGN can usually be measured using the Doppler shift of emission lines ($z = \nu_\mathrm{em}/\nu_\mathrm{obs} - 1$).

Figure 1.4(a) shows a schematic of the geometry of a jet emission region at two separate times of observation. In the rest frame of the AGN, the knot has moved length $l = v\Delta t$ in a time interval Δt. This translates to a projected distance of $s = l \sin\theta = v\Delta t \sin\theta$. The light emitted from the knot at point A (closer to the AGN) will necessarily take longer to reach the observer than light emitted at point B, due to having to travel an added distance of $x = l\cos\theta$. Taking this into account, the observed time interval between points A and B becomes $\Delta t_\mathrm{obs} = \Delta t - x/c = \Delta t(1 - \beta_\Gamma \cos\theta)$

[2] `http://www.astro.ucla.edu/~wright/cosmo_02.htm`

rather than simply Δt. The apparent velocity of the knot is then

$$\beta_{\perp,\mathrm{app}} = \frac{s}{c\Delta t_{\mathrm{obs}}} = \frac{\beta_\Gamma \sin\theta}{(1-\beta_\Gamma \cos\theta)}. \tag{1.4}$$

For a given value of Γ, this relation can be used to determine the angle at which the apparent velocity is maximized − this superluminal angle is where $\cos\theta_{\mathrm{sl}} = \beta_\Gamma$. At this angle, $\sin\theta_{\mathrm{sl}} = \sqrt{1-\cos^2\theta_{\mathrm{sl}}} = \sqrt{1-\beta_\Gamma^2} = 1/\Gamma$. Therefore,

$$\beta_{\perp,\mathrm{app}}(\theta_{\mathrm{sl}}) = \frac{\beta_\Gamma}{\Gamma(1-\beta_\Gamma^2)} = \Gamma\beta_\Gamma = \sqrt{\Gamma^2-1}, \tag{1.5}$$

showing the maximum apparent velocity possible for a given value of Γ. This can then be used to constrain Γ based on the observed apparent velocity, such that

$$\Gamma \geq \sqrt{\beta_{\perp,\mathrm{app}}^2 + 1}. \tag{1.6}$$

A maximum value for the viewing angle θ_{max} can be found using (1.4) by taking the limit where $\Gamma \to \infty$ and $\beta_\Gamma \to 1$, resulting in $\beta_{\perp,\mathrm{app}}^{\mathrm{max}}(\theta) = \sin\theta/(1-\cos\theta)$. Rearranging this and using the observed apparent velocity gives

$$\cos\theta_{\mathrm{max}} = \frac{\beta_{\perp,\mathrm{app}}^2 - 1}{\beta_{\perp,\mathrm{app}}^2 + 1}. \tag{1.7}$$

Thus, the observed apparent superluminal velocity serves as a powerful tool for constraining the jet's bulk Lorentz factor and viewing angle. The application of such constraints to the 3C 111 jet is discussed in §1.8.

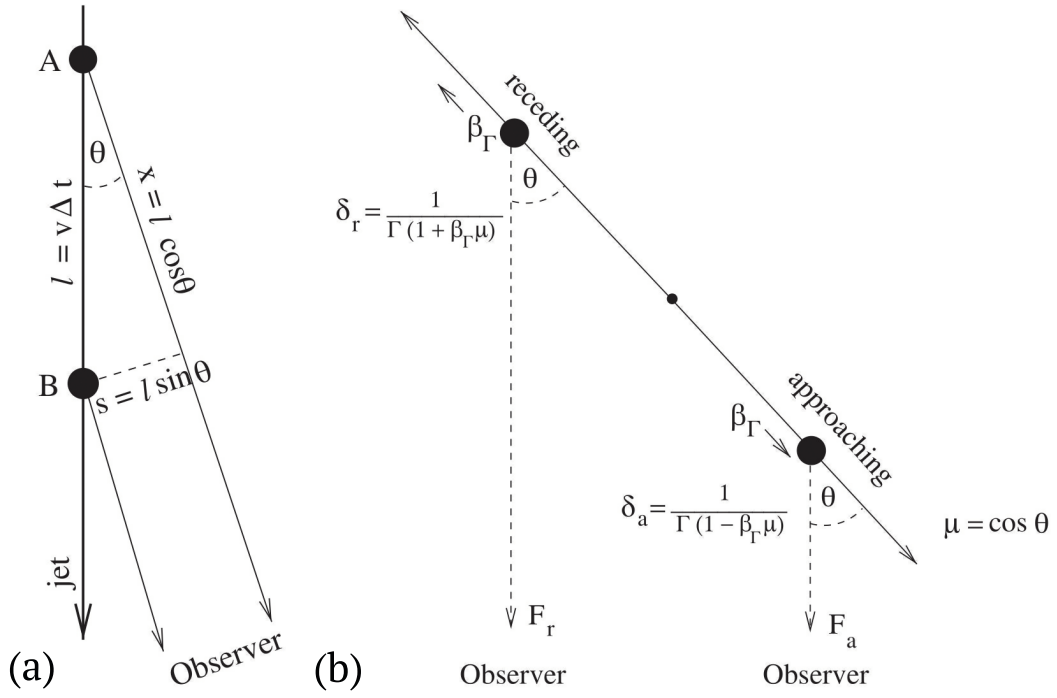

Figure 1.4 (a) Geometry of a jet knot which leads to apparent superluminal motion. (b) Geometry of a two-sided jet. Adapted from Boettcher et al. (2012).

1.5.3 Two-Sided Jets

In some cases, both the jet and counter-jet are detected emanating from an AGN (Figure 1.4b). This is usually when the viewing angle is relatively large, such that the counter-jet is not de-boosted enough to put its flux below the detection limit of our instruments. The flux ratio between components in the jet and counter-jet can be used to constrain the velocity and viewing angle of the jet. Doing so, however, relies on the assumptions that the components in each side of the jet are emitting the same luminosity istropically as each other, that each component is moving at the same velocity, and that the jet and counter-jet are 180° apart. These are rather large assumptions that are unlikely to be strictly true, and so in general the values this method points to are less trustworthy than those provided by the superluminal motion method described in the previous section. In particular, the light emitted by the receding component may take many thousands

of years longer to reach the observer than light from the approaching component, and so the stage of the development that we observe in each is unlikely to be the same. This method, however, can be applied even on large scales, where apparent motion is not superluminal or even detected, including all the way out to the hotspots.

As shown in (1.3), we can use the Doppler factor to determine the amount by which the emitted flux is boosted in the receiving frame. Assuming the flux of the two jet/counter-jet components are equal to F_0, it follows that

$$F_{\rm a,r} = F_0 \delta_{\rm a,r}^{3+\alpha}, \tag{1.8}$$

where the "a" and "r" subscripts denote the approaching and receding jet components, respectively. The Doppler factor for each of the components, accounting for the 180° difference in viewing angle, can be expressed as

$$\delta_{\rm a,r} = \frac{1}{\Gamma(1 \mp \beta_\Gamma \cos\theta)} \tag{1.9}$$

where θ is the viewing angle between the approaching jet and the line-of-sight. Using these equations to take the flux ratio of the approaching and receding components yields

$$\frac{F_{\rm a}}{F_{\rm r}} = \left(\frac{1 + \beta_\Gamma \cos\theta}{1 - \beta_\Gamma \cos\theta}\right)^{3+\alpha}. \tag{1.10}$$

We apply this method for the approaching and receding hotspots of the 3C 111 jet in §4.2, with one difference. Since we were considering the hotspot flux ratio, we used a factor of $\delta^{2+\alpha}$ (for a steady state or slow-moving structure) in lieu of the above $\delta^{3+\alpha}$ (for a spherical component moving at relativistic speeds). The extra factor of δ comes from the relativistic time compression. This choice is common when considering hotspots as they are more likely to be slow-moving rather than ultra-relativistic (e.g., Hardcastle et al. 2016). The difference, however, is minor given that hotspots generally have a

velocity of $\beta_\Gamma < 0.3$ (e.g., Longair & Riley 1979), corresponding to a Doppler factor of $\delta \lesssim 1.2$.

Another diagnostic that can be used on two-sided jets is that of the arm-length ratio. The distance between the AGN core and the hotspots of the jet and counter-jet, after accounting for the light-travel time difference between the two hotspots, can be used to roughly determine the hotspot advance velocity − the speed at which the hotspots are plowing through the IGM (Ryle & Longair, 1967; Blundell & Alexander, 1994). While this is not a direct diagnostic of the jet's speed, it can be used to roughly constrain a minimum velocity for the jet before decelerating when interacting strongly with the IGM. One would expect the approaching jet to have a larger apparent length than the receding jet provided the viewing angle is sufficiently less than 90°, as it is seen at a later stage of development due to it being closer. The derivation is equivalent to that of the observed time interval in the case of superluminal motion in a jet, but now applied both for approaching and receding jets, such that

$$\Delta t_{\rm obs}^{\rm a,r} = \Delta t(1 \pm \beta_\Gamma \cos\theta). \tag{1.11}$$

The arm-length ratio can then be found by

$$\frac{l_{\rm a}}{l_{\rm r}} = \frac{c\Delta t_{\rm obs}^{\rm a}}{c\Delta t_{\rm obs}^{\rm r}} = \left(\frac{1+\beta_\Gamma \cos\theta}{1-\beta_\Gamma \cos\theta}\right). \tag{1.12}$$

Typical values for the arm length ratio are $\lesssim 1.5$, though they can be larger (e.g., Konar et al. 2008). We use the arm-length ratio of the 3C 111 jet and counter-jet to estimate the hotspot advance velocity in §4.2.

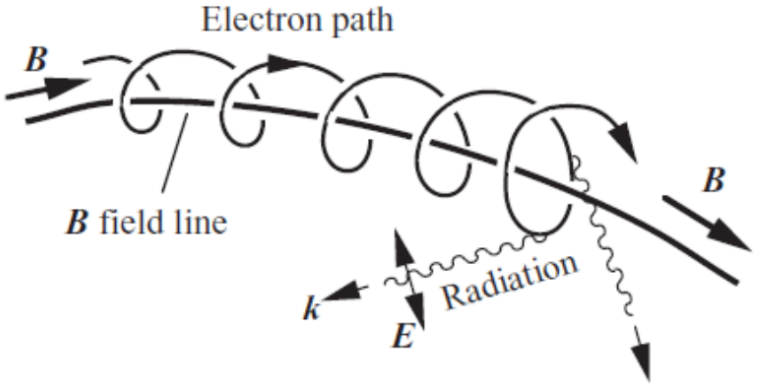

Figure 1.5 Synchrotron radiation produced as an electron spirals along a magnetic field line. From Bradt (2014).

1.6 Non-thermal Radiative Processes

The primary mechanism for electromagnetic radiation in jets is that of synchrotron emission, however the presence of relativistic electrons in a photon field guarantees that inverse-Compton scattering will occur. Due to the relatively low particle densities in jets ($n \lesssim 10^3$ cm^{-3}), other effects due to particle collisions (e.g., Bremsstrahlung, Coulomb scattering, pair annihilation) are not thought to be important. In this section, Greek letters will correspond to properties of individual particles rather than to the bulk properties of the jet.

1.6.1 Synchrotron Radiation

A charged particle, such as an electron, will emit electromagnetic radiation as it is accelerated in a spiral trajectory by a magnetic field (Figure 1.5). When the particle is moving at relativistic speeds, this is known as synchrotron emission. This process is

ubiquitous in nature and present throughout jets. A single particle will emit a synchrotron spectrum that is strongly peaked near the critical frequency

$$\nu_{\rm c} = \left(\frac{3qB}{4\pi mc}\right)\gamma^2, \tag{1.13}$$

where q is the charge of the particle, B is the magnetic field strength, m is the mass of the particle and the Lorentz factor $\gamma = E/(mc^2)$, with E being the particle's energy. The total emitted power, over all frequencies, is

$$P_{\rm syn} = -\frac{dE}{dt} = \frac{2}{3} r_{\rm e}^2 c \beta_\perp^2 \gamma^2 B^2. \tag{1.14}$$

(e.g., Rybicki & Lightman 1979). For an isotropic distribution of particles each with speed β, we can then average over all pitch angles ψ, where the pitch angle is the angle between the field and velocity, so that

$$< \beta_\perp^2 >= \frac{\beta^2}{4\pi} \int \sin^2\psi \; d\Omega = \frac{2}{3}\beta^2. \tag{1.15}$$

Plugging this in gives us the total power as

$$P_{\rm syn} = \left(\frac{2}{3}\right)^2 r_{\rm e}^2 c \beta^2 \gamma^2 B^2, \tag{1.16}$$

or

$$P_{\rm syn} = \frac{4}{3}\sigma_{\rm T} c \beta^2 \gamma^2 u_{\rm B}. \tag{1.17}$$

Here, $\sigma_{\rm T} = 8\pi r_{\rm e}^2/3$ is the Thomson cross section and $u_{\rm B} = B^2/(8\pi)$ is the magnetic energy density.

An important note is that since $r_{\rm e} = e^2/(mc^2)$, we have $P_{\rm syn} \propto m^{-2} \Rightarrow dE/dt \propto -m^{-2}$. Thus, the energy-loss rate is strongly dependent on the mass of the particle. For a proton to suffer the same energy-loss rate as an electron with Lorentz factor $\gamma_{\rm e}$, its

Lorentz factor would need to be $\gamma_{\rm p} \approx (1836)^2 \gamma_{\rm e}$, and its energy would need to be larger by a factor of $(1836)^3$. Therefore, electrons are much more efficient radiators than are protons, with a larger power output and consequently a much shorter radiative lifetime.

A particle distribution $n(\gamma)$ can be defined by

$$n(\gamma) = n_0 \gamma^{-p}, \tag{1.18}$$

where $n(\gamma)$ is the number of particles per unit volume in a Lorentz factor interval $[\gamma, \gamma + d\gamma]$, and p is the power law index of the distribution. The particle energy distribution can be expressed as

$$N(E)dE = CE^{-p}dE \tag{1.19}$$

for an energy range $E_1 < E < E_2$. The power law index p of the particle spectrum is related to the power law index of the photon spectrum by

$$P_{\rm tot}(\nu) = \int \left(-\frac{dE}{dt}\right) N(E)dE \propto \nu^{-(p-1)/2}, \tag{1.20}$$

such that

$$\alpha_{\rm syn} = \frac{p-1}{2} \tag{1.21}$$

The synchrotron emission coefficient, for a given particle distribution $n(\gamma)$, can be stated as

$$j_\nu = \frac{1}{4\pi} \int_1^\infty d\gamma \; n(\gamma) \; P_\nu(\gamma). \tag{1.22}$$

In the observer's frame, accounting for all the various relativistic aberrations, the radiative power per unit frequency of synchrotron emission from a particle will be

$$P_{\rm syn}(\nu) = \frac{\sqrt{3} q^3 B}{mc^2} \sin\psi \; F\left(\frac{\nu}{\nu_{\rm c}}\right) \tag{1.23}$$

(e.g., Rybicki & Lightman 1979).

1.6.2 Inverse-Compton Scattering

Inverse-Compton scattering is an interaction between a relativistic particle and a photon in which the particle imparts some of its energy into the photon, increasing its energy/frequency. Within an emission region of the jet, multiple scatterings of a given photon are very unlikely due to the small optical depth ($\tau_{\rm C} \lesssim 10^{-5}$), though exceptions do exist. An important part of inverse-Compton scattering is the Compton cross-section. Depending on the energy of the photon relative to that of the scattering electron, the cross section can change significantly, such that

$$\sigma_{\rm C}(\epsilon') \approx \begin{cases} \sigma_{\rm T}\left(1 - 2\epsilon' + \frac{26}{5}\epsilon'\right) & \text{for} \quad \epsilon' \ll 1 \\ \frac{3}{8}\frac{\sigma_{\rm T}}{\epsilon'}\left(\ln[2\epsilon'] + \frac{1}{2}\right) & \text{for} \quad \epsilon' \gg 1. \end{cases} \tag{1.24}$$

Here, $\epsilon \equiv h\nu/(m_{\rm e}c^2)$ is the energy of the photon in units of the electron's rest-mass energy (before scattering), the primed superscript indicates the quantity is being measured in the electron's rest frame before scattering (Figure 1.6). The Compton cross-section matches well the Thomson cross-section for small values of $\epsilon' \ll 1$, where the photon energy is far below that of the electron's rest-mass energy; this is called the Thomson regime. Photons scattered in this regime have a scattered photon energy $\epsilon'_{\rm s}$ nearly equal to the incident photon energy ϵ', or $\epsilon'_{\rm s} \approx \epsilon'$. In the Lab frame, however, the scattered photon energy will be $\epsilon_{\rm s} \sim \gamma^2\epsilon$, which represents an energy transfer from the electron to the proton. When the electron is highly relativistic ($\gamma \gg 1$), the energy the photon receives can be very large, capable even of boosting CMB photons from microwaves to X-rays.

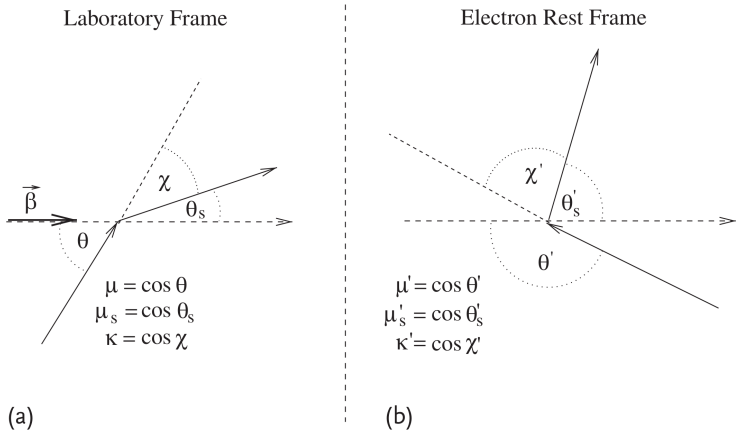

Figure 1.6 Compton scattering geometry for (a) the Lab frame and (b) the electron's rest frame. From Boettcher et al. (2012).

The limit where $\epsilon' \gg 1$ is known as the Klein-Nishina limit, and is the regime in which the energy transfer from the photon to the electron can be significant.

The total Compton power is given by

$$P_{\rm Comp} = \frac{4}{3}\sigma_{\rm T} c \beta^2 \gamma^2 u_{\rm rad}, \tag{1.25}$$

where $u_{\rm rad}$ is the energy density of the radiation field. This equation for Compton power is nearly identical to that of the synchrotron power (1.17). This is because both processes are fundamentally the same type of interaction, between that of a photon and a charged particle. In the case of synchrotron self-Compton (SSC), where synchrotron-emitted photons are Compton scattered by their own seed electron population, it follows that

$$\frac{P_{\rm Comp}}{P_{\rm syn}} = \frac{u_{\rm rad}}{u_{\rm B}}. \tag{1.26}$$

1.7 Particle Acceleration

The radiative lifetime of a particle is such that $\tau \propto \nu^{-1/2}$ (e.g., Boettcher et al. 2012), so that all but the lowest energy electrons will lose their energy long before reaching the hotspot (Harris & Krawczynski, 2007). *In situ* particle acceleration is necessary to explain the observed emission in jet knots and hotspots.

There are many possible ways in which particle acceleration can occur in jet knots. Fermi acceleration is one such process in which the particles can be accelerated either by an interaction with the external ISM or, more favorably, by particles interacting back-and-forth across a shock boundary. However, efficient Fermi acceleration cannot take place when the shocks are relativistic, which is thought to be common in the case of jets (Sironi et al., 2015).

Magnetic reconnection is increasingly thought to play a large role in jet particle acceleration (Zweibel & Yamada, 2009). In a plasma where conditions are such that the magnetic field lines are not "frozen in" (even temporarily), and provided the magnetic field is strong enough, the field lines can change their topology in such a way that magnetic field energy is then converted into bulk kinetic energy resulting in a burst of particle acceleration. In general, this is thought to be a very efficient method of particle acceleration. However, magnetic reconnection is only expected to take place when the magnetic field energy density exceeds that of the particle energy density. This has the advantage of explaining how a Poynting flux-dominated jet, when launched, can later come to be in equipartition between magnetic field energy and bulk kinetic energy in an efficient way (Sironi et al., 2015).

1.8 The Jet of 3C 111

The 3C 111 jet is an FR II and one of the longest jets known, with an angular size of $\sim$2 arcmin on its approaching side. The counter-jet has not been detected aside from its hotspot. Sargent (1977) first determined the redshift of 3C 111 to be $z = 0.0485$ by measuring the Doppler shift of several emission lines. The corresponding scale is 0.956 kpc/arcsec. Due to a low galactic latitude of $-8°.82$, observations of 3C 111 suffer from a considerable amount of extinction, as well as a relatively crowded field.

Jorstad et al. (2005) used VLBI observations over a period of several years and analyzed the proper motion of observed approaching jet components to determine the most likely parsec-scale parameters to be $\theta = 18°.1 \pm 5°.0$, $\Gamma = 4.4 \pm 1.3$, and $\delta = 3.4 \pm 1.1$. Oh et al. (2015) more recently used VLBI observations to constrain the viewing angle of 3C 111 on mas scales to $\theta \lesssim 20°$ and the intrinsic velocity to $\beta \gtrsim 0.98$, in agreement with the findings of Jorstad et al. (2005).

Prior to this project, the optical emission from the jet was undiscovered aside from the emission from the approaching hotspot (Meisenheimer et al., 1997). The X-ray emission from the jet was discovered by Hogan et al. (2011), though this was only a 9 ks observation using *Chandra* and provided too few counts in the jet to do significant science with.

1.9 Motivation

The first observations with *Chandra* detected excess X-ray flux in the jet of PKS 0637-752 that could not be explained by a single power-law from radio to X-ray; a second emission component was required. Tavecchio et al. (2000) first made the case that the second emission component was due to inverse-Compton scattering of an external

seed photon field, namely that of the Cosmic Microwave Background (CMB). For over a decade, the so-called EC/CMB (or IC/CMB) mechanism has been the dominant explanation for the detected X-ray flux in FR II jets; for FR I jets, a single power-law component is sufficient (e.g., Hardcastle et al. 2001). In fact, the analysis of the original *Chandra* observation of the 3C 111 jet made the assumption that the emission was due to EC/CMB (Hogan et al., 2011).

The CMB is unique as a seed photon field because its density increases with cosmological redshift, such that its boosted energy density (in the jet frame) is

$$u'(\mathrm{CMB}) = 4 \times 10^{-13}\ (1+z)^4\ \Gamma^2\ \ \mathrm{erg\ cm^{-3}}, \tag{1.27}$$

(e.g., Harris & Krawczynski 2006). Consequently, EC/CMB is much more likely to be dominant in jets at large redshifts than in those nearby. It also has the advantage of being a mandatory process, and only requires a single population of electrons.

However, there are serious drawbacks to such a model. In particular, it demands a highly relativistic jet with bulk Lorentz factor $\Gamma \sim 10$ over distances of perhaps hundreds of kpc (since an inverse-Compton-scattered photon is boosted by a factor of $\sim \gamma^2$). EC/CMB also requires a very small viewing angle to the observer, so that the Doppler factor is very high, to explain the observed X-ray flux in many jets. It also often demands a jet kinetic power in excess of the Eddington limit.

Another possible explanation for the detected X-ray emission is that of synchrotron emission from a second population of relativistic electrons. This model does not require the jet to be highly relativistic or to have a small viewing angle. It does, however, require extremely efficient particle acceleration *in situ* along the large-scale jet.

In recent years, EC/CMB has been ruled out as the dominant X-ray emission process in several jets. Meyer & Georganopoulos (2014) used *Fermi* observations to put

an upper limit on the gamma-ray flux from the jet of 3C 273 − they found an upper limit that is below the flux predicted by the EC/CMB model. The authors have applied the same technique to rule out EC/CMB for PKS 0637-752 (Meyer et al., 2015). Cara et al. (2013) used optical *HST* polarimetry of PKS 1136-135 to rule out EC/CMB − synchrotron emission is naturally polarized to a much higher degree than that predicted by EC/CMB. Hardcastle et al. (2016) primarily focused on the jet/counter-jet flux ratio (Equation 1.10) to show that the jet of Pictor A is not relativistic enough for EC/CMB to explain the observed X-ray emission − however, this method makes the assumption that the jet and counter-jet are intrinsically identical and 180° apart.

Despite these recent results, the dominant X-ray emission mechanism in FR II jets is still in dispute (e.g., Liu 2015). Our hope with this project and future observations is to use 3C 111 as an ideal test-case to constrain the X-ray emission mechanism in an FR II jet due to its unique properties.

Chapter 2

Observations and Data Reduction

2.1 Near-IR/Optical/UV

In this section is described our new and archival Hubble Space Telescope (*HST*) data and the various data reduction techniques that were used to improve the data quality. *HST* is a space telescope with a primary mirror of diameter 2.4 m and several instruments specializing in near-IR through UV observations with good spatial resolution and sensitivity.

2.1.1 Observations

Observations in several bands were acquired using *HST* (Table 2.1). *HST* observations were conducted using the Wide Field Camera 3 (WFC3) using the IR and UVIS channels; archival data taken by the Wide Field Planetary Camera 2 (WFPC2) was also used. WFC3 was installed in May 2009 as a replacement for the aging WFPC2 instrument, featuring a larger field of view and a large improvement in sensitivity. Its design is such that it provides a very large field of view (123 x 136 arcsec for IR, 162 x 162 arcsec

for UVIS) and allows for a broad wavelength coverage (from 200 to 1700 nm) (Dressel, 2015). These features make WFC3 well-suited to multiwavelength observations of an extended jet such as 3C 111. An archival observation of within ∼20 arcsec of 3C 111 using the Near Infrared Camera and Multi-Object Spectrometer (NICMOS) did not detect any part of the jet and was not used.

For our WFC3/IR observations, the F160W filter was used. The IR channel has the advantage of low dark current ($\sim$ 0.048 e^-/s/pixel) and read noise ($\sim$ 12.0 e^-), as well as being good at filtering out cosmic rays due to its *MULTIACCUM* mode - instead of a single read, the detector conducts a series of non-destructive reads. The IR detector does not have a mechanical shutter; the charge on the detector is instead reset when a new exposure is to be taken. The process of a *MULTIACCUM* readout is as follows: first, the charge of each pixel is reset (to the bias level), then the array is read as quickly as possible to create a zero read image, followed by up to 15 reads with each frame being stored individually in the on-board memory of the computer. Each frame is able to be used to remove cosmic ray strikes and decreases the likelihood of pixel saturation − saturation is when a pixel collects too many photoelectrons which end up bleeding over into nearby pixels.

WFC3/IR has rectangular pixels of size 0.135 x 0.121 arcsec/pixel. WFC3/IR is able to image point spread functions (PSFs) very tightly, making it prone to PSFs that are undersampled. For the IR detector, the ratio between the PSF full width at half maximum (FWHM) and the pixel scale is about 1.0 to 1.25. A ratio below 1.5 is considered undersampled, meaning that spatial information is lost (Howell et al., 1996). What follows from the Nyquist theorem (Nyquist, 1928) is that a ratio of 2 or better is desired for ideal sampling of the PSF, meaning that the FWHM of the PSF should be about 2 pixels on the image, such that the Gaussian nature of the PSF is apparent. Dithering the observations (described below) and using the Drizzle algorithm (described

in §2.1.2.1) allow for the pixel scale to be reduced by a factor of ∼0.5, which would put the sampling ratio at about the ideal range. Figure 2.1 shows how undersampling can lead to dramatic loss of spatial information.

Since the approaching jet of 3C 111 is roughly 2 arcminutes in length, two fields were chosen for the IR observations - one aimed at the approaching jet, and one to cover the receding side to observe the counter-jet hotspot. Dithering was used on each field, wherein two exposures are taken with an offset of 3.5 pixels from one another. The combination of two dithered images allows for a better sampling of the PSF as well as aiding in the removal of any detector artifacts (such as hot pixels) and any remaining cosmic ray flux not handled by the incremental readouts of the detector. In total we collected four IR images, with most of the overlap being in the half of the jet closest to the AGN core. WFC3 images suffer from significant geometric distortion - each detector must be tilted with respect to its optical axis (∼24° for IR, ∼21° for UVIS) in order to keep them in constant focus. The tilt combined with the variation of plate scale across the detector amounts to about a 4% variation from one corner of an IR image to the other (Rajan et al., 2010). The correction of these geometric distortions is handled by the `AstroDrizzle` package (discussed in §2.1.2).

For our WFC3/UVIS observations, the F850LP filter was applied. The UVIS detector has a plate scale of ∼0.03962 arcsec/pixel. The dithering strategy chosen for this detector utilized a 2.5 pixel offset between exposures. The sampling ratio for UVIS is already between 1.6 and 2.3, so dithering and the subsequent subsampling is less important than with WFC3/IR for the PSF, but crucial for eliminating cosmic ray strikes. Like the IR detector, the UVIS CCD has the advantage of very low read noise ($\sim 3.2\ e^-$) and dark current ($\sim 7\ e^-$/hr/pixel), however it suffers from several problems not found in the IR detector. In particular, the detector suffers from charge transfer efficiency (CTE) degradation (Baggett et al., 2012). A perfect detector would be able to

Table 2.1. Relevant information for the *HST* data analyzed

Instrument	**Exposure Time (s)**	**Central Wavelength (Å)**	**Obs. Date**
WFC3/IR/F160W	5211	15369.176	01/30/2013
WFC3/UVIS/F850LP	2534	9167.321	01/30/2013
WFPC2/F791W[a]	34200	7881	02/26/1996

[a]Approaching hotspot centered on PC chip.

transfer 100% of the charges stored in each pixel during readout. However, in practice, traps within the lattice of the CCD will temporarily retain some of the electrons and release them over the course of several seconds. This results in streaks that can be seen in the image trailing away from bright pixels. Though the UVIS detector was designed to minimize CTE losses, the problem tends to get worse over time thanks to the inhospitable environment in which *HST* exists.

Only one field was used for the UVIS observation due to its large field of view, which included the jet and receding hotspot but just missed the approaching hotspot due to the unfavorable orientation angle. Dithering was used, as with the IR, to give us two UVIS images in total. The small number of images made it difficult to isolate and remove cosmic ray strikes including a significant number that occur in the same pixels on both exposures. CTE streaks and cosmic rays were a significant problem with this data set (discussed in §2.1.2).

The archival WFPC2 observations were taken with the F791W filter. This observed field primarily included the NHS and most of the outer jet, however due to the relatively low sensitivity of the instrument only the NHS is detected. WFPC2 is composed of three wide field chips and a single higher-resolution chip. The wide field chips have plate scales of 0.1 arcsec/pixel while the Planetary Camera (PC) chip has a scale of 0.046 arcsec/pixel (McMaster et al., 2008).

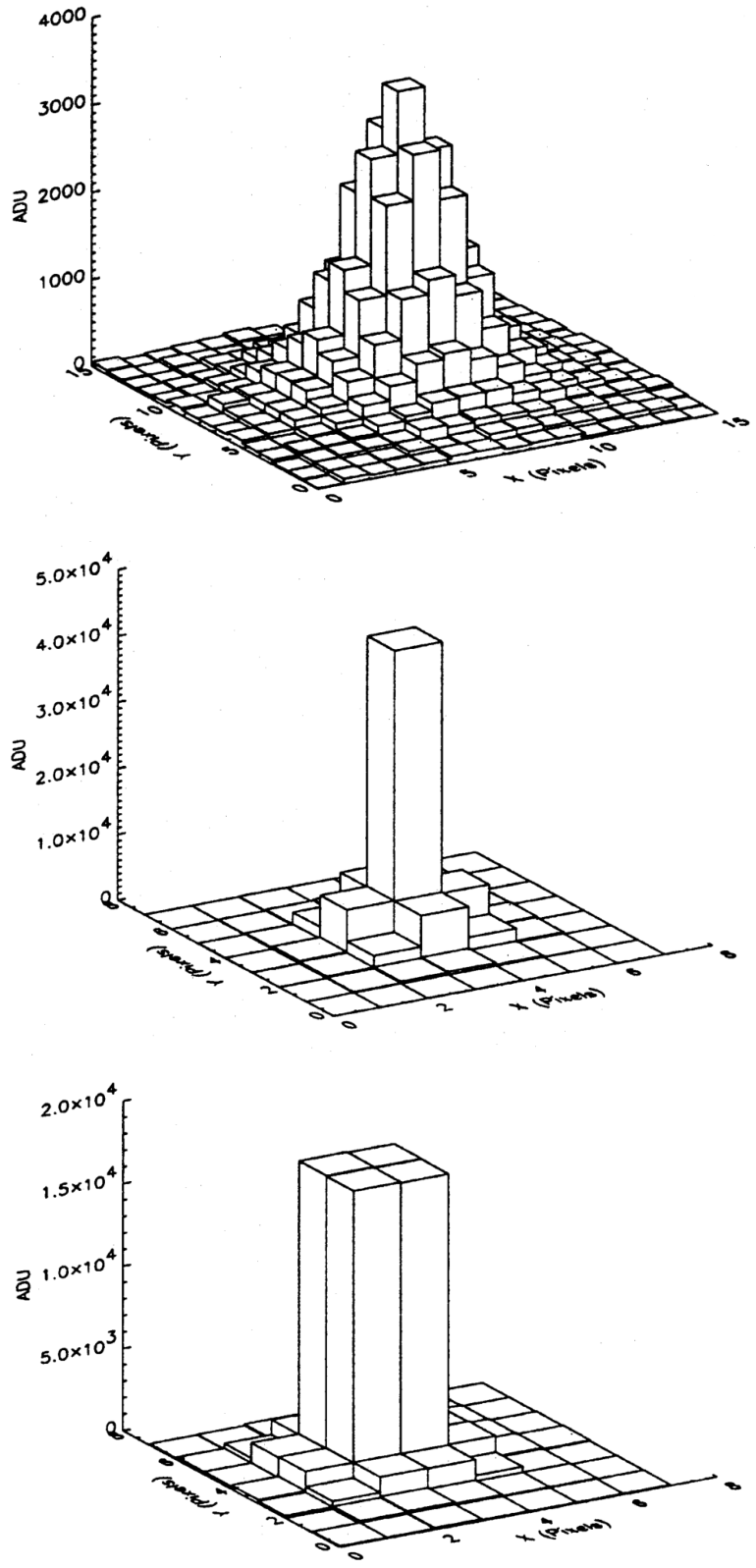

Figure 2.1 The same PSF is shown in each panel with varying degrees of sampling ratio and position on the detector (reproduced from Howell et al. 1996).

2.1.2 Data Reduction

The data reduction techniques that were used differed between each *HST* data set, and so each has been given its own sub-section.

2.1.2.1 WFC3/IR + F160W

The data reduction for our *HST* observations was done primarily with the Image Reduction and Analysis Facility (IRAF), its Python-integrated spinoff known as PYRAF, and the Python programming language. When requested for download, *HST* data are processed using On-The-Fly-Reprocessing (OTFR), which incorporates the use of `calwf3` and `MultiDrizzle` − software written by STScI for use in calibrating and processing HST images (Rajan et al., 2010). `calwf3` is used in the pipeline process to handle the necessary calibration steps, while `MultiDrizzle` (and its successor `AstroDrizzle`) can be used manually to adjust the specific parameters of image processing and whose main purpose is to align and combine *HST* images; both of these are included in a software package called `DrizzlePac`, which also includes various other programs for handling *HST* data. The individual **raw** exposures are processed by `calwf3` to give the calibrated **flt** files. The steps involved with this include flagging bad pixels in the data quality (DQ) array, subtracting off the bias, dark image and read noise (described below), correcting for photometric non-linearity and calculating the photometric values needed for flux conversion, and flat-fielding and applying the gain. The bias image is usually an image taken with an exposure time of zero seconds; it allows for determining the noise level within each frame. The bias for WFC3/IR is determined using the science exposure itself rather than a separate zero-second exposure because of the nature of the *MULTIACCUM* mode it uses. The method used relies on five rows of reference pixels that surround the detector, which are insensitive to light and measure the bias level at the time of each readout − the mean value of each readout bias is calculated and

subtracted from the science pixels for that read. Dark current is the thermal noise from the CCD itself and tends to increase linearly with time. For WFC3/IR, dark current calibration files are created on a regular basis throughout each cycle. `calwf3` uses the associated dark frame, scales it, and subtracts it from each science image. Flat fielding is the process in which the telescope is exposed to a light source of uniform brightness, such as a lamp or a white wall; this is done to correct for pixel-to-pixel variations in the CCD response and account for any nonuniform sensitivity of the detector. The flat field images used by WFC3 were created in 2008 while it was still on the ground. These are supplemented by in-orbit "L-flats" which are created by exposing different parts of the detector to the same bright region of stars in the globular cluster Omega Centauri. These are then multiplied into the ground-based flat field image and that is what is used by `calwf3` for processing.

After this, the `tweakreg` tool (part of the `DrizzlePac` package) was used to improve the alignment of the various **flt** files. When mosaicing images, it is vitally important that the header of each file includes World Coordinate System (WCS) information that is aligned to sub-pixel accuracy. `Tweakreg` allows for the alignment of several images to one another or to an external reference image. The `AstroDrizzle` task was then used to mosaic the images for each filter. The linchpin of `AstroDrizzle` is the variable-pixel linear reconstruction algorithm, better known as Drizzle. By drizzling multiple dithered images, a closer approximation of the "true sky" image can be recovered (Gonzaga et al., 2012). Drizzling allows for the pixel size to be shrunken using the pixfrac parameter before it is averaged onto the output image. The shrunken pixels are aligned and geometrically corrected before being "drizzled" onto the subsampled pixel grid (shown in Figure 2.2). The flux from each input pixel is divided up proportionally to how much of its area was drizzled onto the subsampled image. In practice, the Drizzle algorithm has shown good success in recovering information that is lost due to the finite size of detector pixels (Figure 2.3). `AstroDrizzle` must account for the differences in

exposure time between each combined image and also factor in the drizzling process to create a weight map. `AstroDrizzle` also corrects the geometric distortions in the final output image and removes cosmic rays by comparing the various exposures.

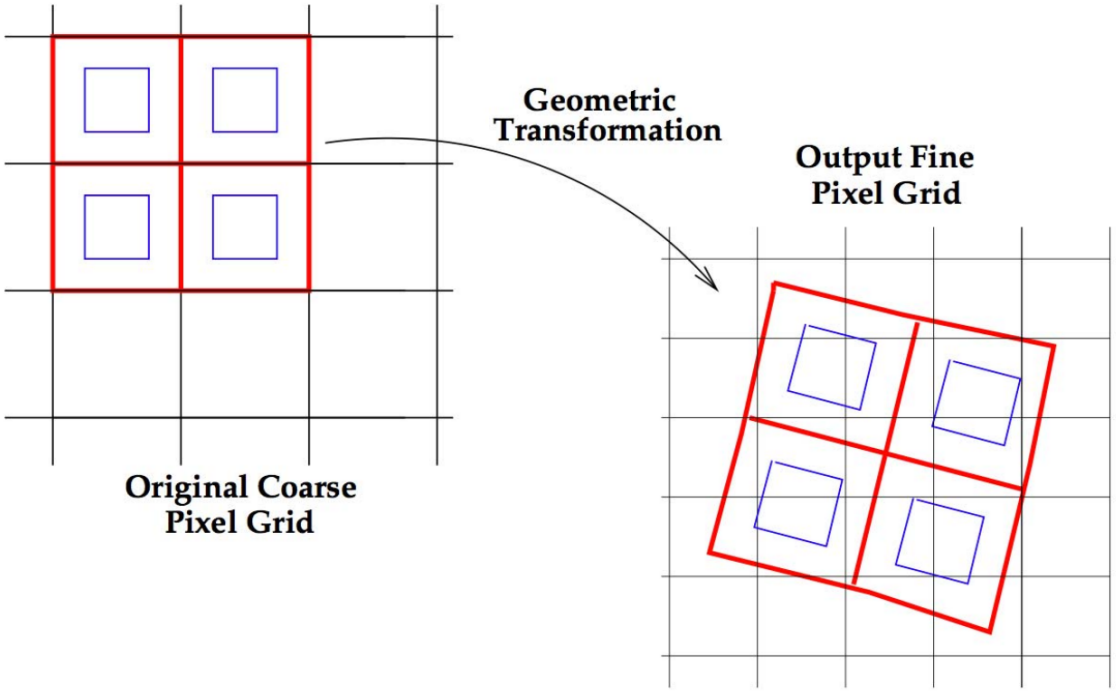

Figure 2.2 Schematic representation of how Drizzle maps input pixels onto the output image. The pixfrac parameter controls the size ratio between the original (red) pixel size and the shrunken (blue) pixel sizes used to distribute the flux onto the output image (Gonzaga et al., 2012).

Below, we highlight some of the important parameters we used in `AstroDrizzle` for our data set.

SKY SUBTRACTION: The method we found that worked best was to use the "match" algorithm included in the development version of `DrizzlePac 2.0` (Avila et al., 2015). This is a newly-implemented method for matching the sky between chips and exposures. Previous methods were problematic for our observations because they relied on the edge of each image to be free of stars and other sources of emission – since our field is littered with many stars and distant galaxies, as well as four bright galaxies

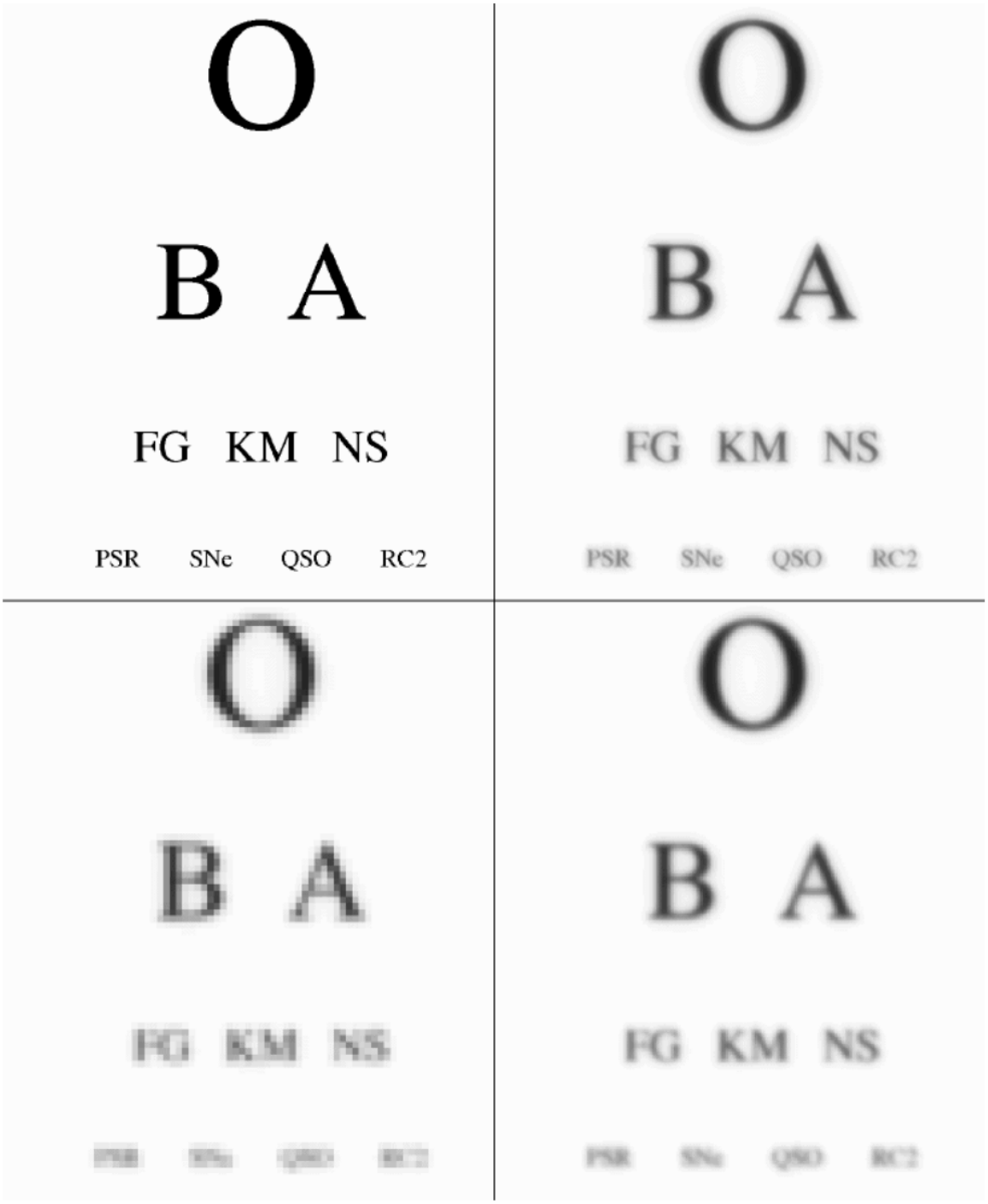

Figure 2.3 *Upper Left*: A "true" image as seen by a telescope of infinite aperture. *Upper Right*: The "true" image convolved with the *HST*/WFPC2 PSF. *Lower Left*: The effect of sampling the convolved image with the WF2 CCD. *Lower Right*: The result of using the Drizzle algorithm to recover information lost due to sampling (Gonzaga et al., 2012).

(probably) in the same group as 3C 111, the edges of each exposure were not reliable for finding the background sky values. The improved matching algorithm determines the differences in sky values in common regions of each exposure.

PIXFRAC: The pixfrac parameter determines how the input pixels should be scaled before being drizzled onto the output image. Setting this value to 0 is equivalent to using the interlacing method of combining images, while setting it to 1 is equivalent to the shift-and-add method. In general, a lower pixfrac value will result in higher resolution and lower correlated noise, but a reduced sensitivity to faint features. The DrizzlePac Handbook suggests leaving the parameter set to 1 for the individual drizzling of each exposure, as this helps with cosmic ray rejection, and then using a minimum fraction of 0.7 when combining the drizzled exposures into the final output image to ensure good coverage. The linear ratio used will depend on the number of images one is combining. In our case for F160W, we have 4 images to combine, and through trial and error found a pixfrac of 0.75 to be best. Using a pixfrac of 0.7 or lower resulted in some scattered pixels that had no flux from the input images.

PIXEL SCALE: The smallest recommended pixel scale is half of the plate scale. In practice, we found this to give the best result as well, and so our pixel scale was set to 0.0642 arcsec/pixel.

After the images were mosaicked, we then updated the WCS coordinates to be more accurate. We used the radio position of 3C 111, determined from an archival VLA image (Leahy et al., 1997), to calibrate its position on our *HST* image. The Astronomical Image Processing System (AIPS) task known as `jmfit` was used to find the pixel value of the center of 3C 111's core. It does so by fitting Gaussian components to the image and using those to find the peak; our image was unaffected by saturation for reasons already described, allowing the Gaussian-fitting process to work well. This is similar to the process used by the IRAF task `imexam`, however AIPS was used because it provides

three-decimal precision. Doing so allows us to better compare the IR image with those from X-ray and radio.

Since we are interested in faint jet components near to the core of 3C 111 (which is itself a large galaxy), we performed galaxy subtraction on the image (shown in Figure 2.4). First we created a region mask of all of the various galaxies and stars present in the image to try to isolate only the contribution in flux from 3C 111. Roughly 1300 regions were created in DS9, and were then converted into pixel masks (FITS images with pixel values of 0s and 1s) using a Python script. The STSDAS package in IRAF contains the task `ellipse`[1], which was then used to fit isophotes at varying distances to the galaxy. As part of its input, it takes in the mask so as to exclude most other sources of flux aside from the galaxy itself.

The `bmodel` task was then used to convert the isophote parameters generated by `ellipse` into a FITS image, which was then subtracted from the science image using `imarith` to give a residual output image that (ideally) includes everything except the galaxy's flux contribution. This was done as an iterative process - after the galaxy was subtracted, it makes it easier to see faint sources of flux that can then be excluded before running `ellipse` again. Many iterations of this process were performed, using incremental changes in the exclude mask. The nearby galaxies in the image in particular had a large effect on how well the isophotes were fit. Even small changes to the nearest galaxy's region could have a relatively large effect on several of the isophotes at $\sim$7 arcsec from the core, though this effect was greatly reduced by the method described below.

Because each isophote is determined independently, each is subject to its own systematic error in its intensity. If the pixels used to fit one isophote contain a bit of flux from a star that was not completely masked, then the isophote's intensity will be

[1] `http://stsdas.stsci.edu/documents/SUG/UG_33.html`

slightly larger than that from the galaxy alone. Likewise, if too many pixels are excluded from the fit, `ellipse` will underestimate the flux from the galaxy for that isophote. To reduce the amount of variation between each isophote, we decided to smooth it out by fitting the isophotes to a Nuker law model (Lauer et al., 1995) (shown in Figure 2.5). The isophote table was then edited so that the model values of intensity replaced the original values. The `bmodel` task was used to convert the isophote table into an image, and then the `imarith` task was used to subtract the galaxy model from the original drizzled image. This was successful in smoothing the transitions between isophotes so that they are much less visible by eye. The final WFC3/IR image is shown in Figure 2.6.

2.1.2.2 WFC3/UVIS + F850LP

Much of the data reduction process is the same for WFC3/UVIS as for WFC3/IR, and so this section highlights the key differences between the two. When it comes to the detector itself, WFC3/UVIS is a traditional CCD. For the bias frames, rather than use pixels on the detector itself, WFC3/UVIS performs traditional bias observations. Each month, roughly 120 bias frames are taken and combined into a superbias image, which is then subtracted from the science image (Rajan et al., 2010). Every four days, 10 to 18 dark observations are performed and combined into a superdark image. The dark image is then calibrated with the superbias image and any pixels with values >0.015 electrons/second are flagged as "hot pixels" in the data quality (DQ) file. The process for UVIS also includes the potential addition of using a post-flash image to help reduce charge transfer efficiency (CTE) degradation, however at the time of our observation this hardware capability was disabled.

Before processing the **flt** files with `AstroDrizzle`, we used the `CTE Tools`[2] program, which is written in Fortran, to reduce the effects of CTE degradation (described

[2] `http://www.stsci.edu/hst/wfc3/tools/cte_tools`

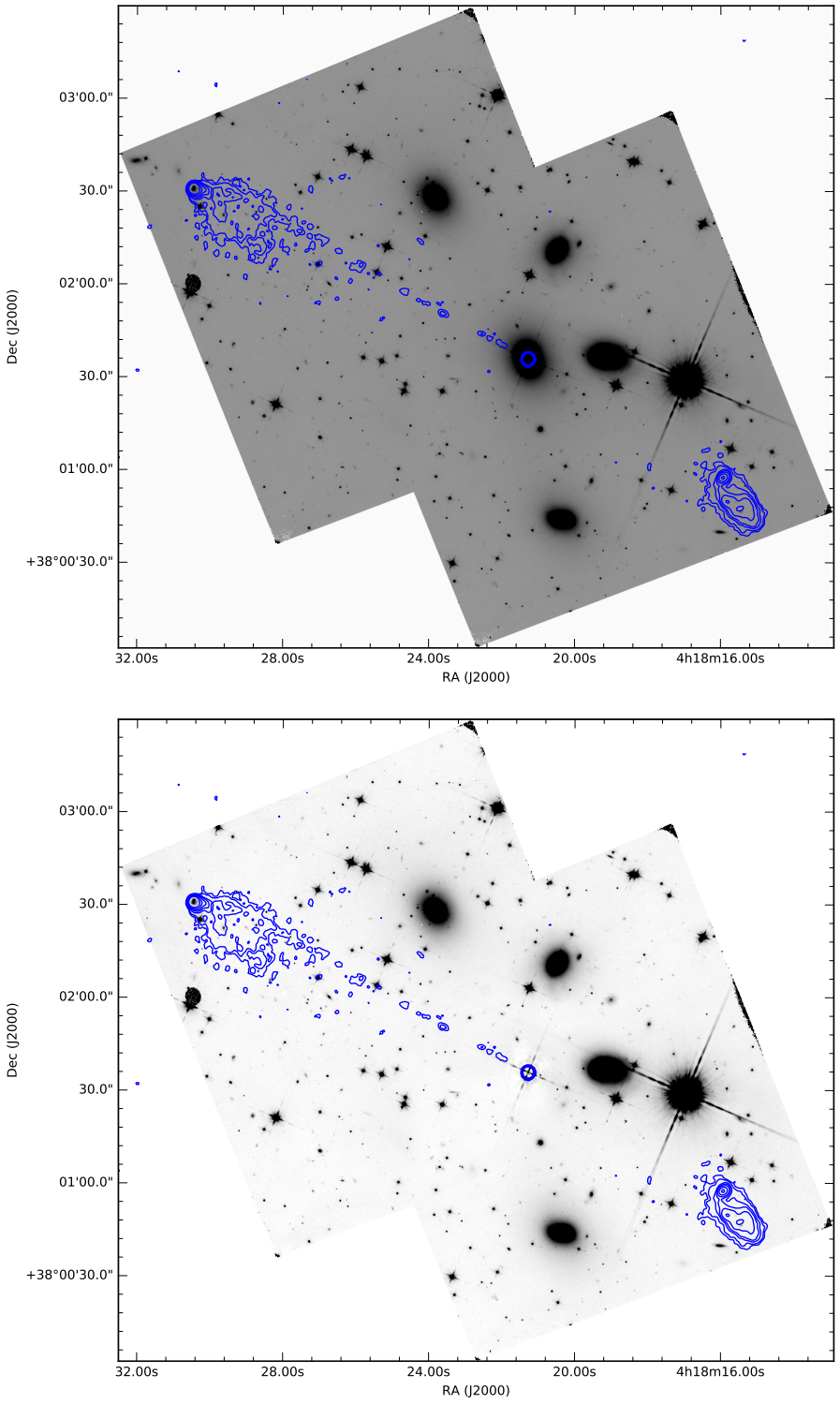

Figure 2.4 The final image for the combined *HST*/WFC3/IR+F160W observations before (*top*) and after (*bottom*) galaxy subtraction was performed (discussed in §2.1.2.1), with radio contours overlaid in blue.

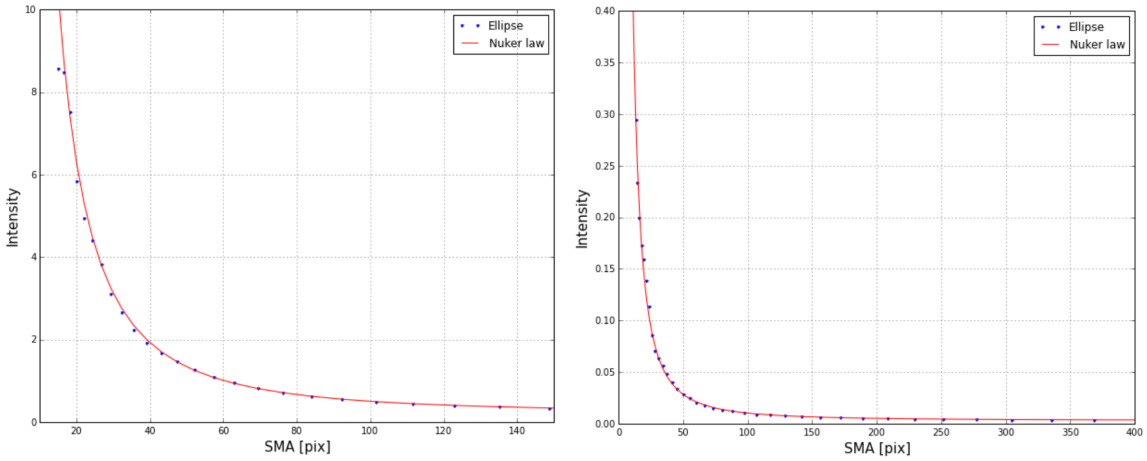

Figure 2.5 3C 111 modeled with a Nuker law for *HST*/WFC3/IR+F160W (*left*) and *HST*/WFC3/UVIS+F850LP (*right*) fit to isophotes generated with the `ellipse` task in IRAF.

previously in §2.1.1). It uses a model algorithm to attempt to reconstruct the smoothest possible image to estimate how charge may have been transferred from pixel to pixel on the actual image (Anderson, 2013). When applied, there was a noticeable improvement in our image, resulting in fewer and shorter streaks caused by CTE degradation; however, many streaks still remained.

The other serious problem we experienced with our WFC3/UVIS data is that of cosmic ray removal. With only two exposures, there were many areas in which cosmic rays impacted the same pixel(s) of the detector on each exposure, making it impossible to recover information from those pixels. To help rectify this, we first used the Python version of the `L.A.Cosmic`[3] program to help identify the cosmic rays. `L.A.Cosmic` uses Laplacian edge detection to detect cosmic rays on a single frame (van Dokkum, 2001). After trial and error adjusting the parameters, we found that this algorithm worked better than the cosmic ray rejection method used by `AstroDrizzle` for most of the cosmic rays present; however, for elongated "streaker" type cosmic ray hits, `AstroDrizzle` did a better job. With that in mind, we decided to use both methods

[3] `http://www.astro.yale.edu/dokkum/lacosmic`

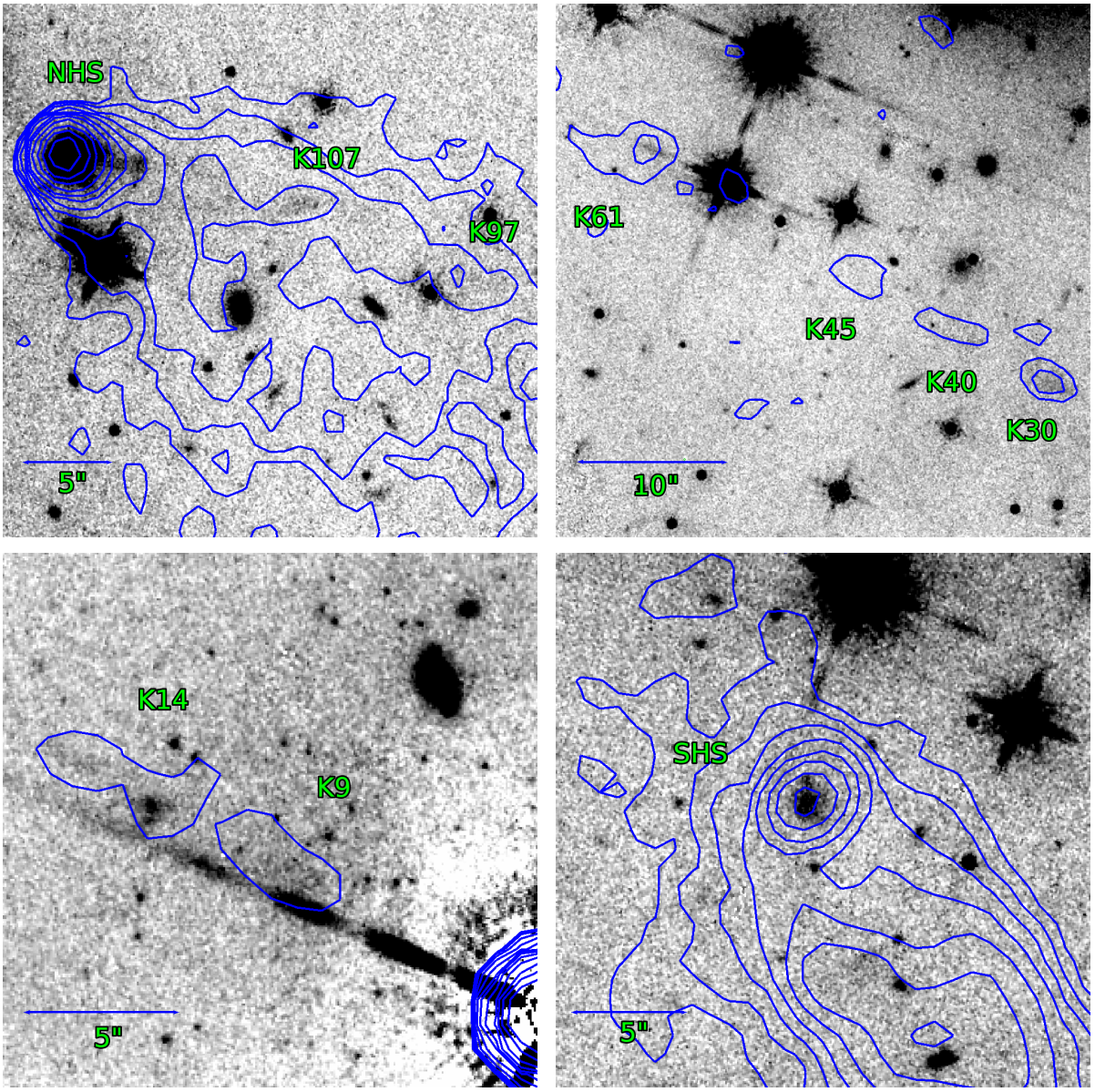

Figure 2.6 Zoomed-in panels of the jet of 3C 111 from the *HST*/WFC3/IR+F160W image. All four panels show the *HST* image in grayscale, with contours from the radio image overlaid in blue. A galaxy model has been subtracted from the HST image (see §2.1.2.1). At top left, we show the brighter, northern hotspot, which is well resolved both parallel to and perpendicular to the jet direction. The top right and bottom left images show the inner part of the northern jet, specifically the part extending from about 5 arcsec to about 65 arcsec from the nucleus. The bright linear feature in the bottom left panel is a diffraction spike from the AGN nucleus. At bottom right, we show the fainter, southern hotspot, which is also well resolved. The X-ray detected knots have been labeled in green (see Figure 2.10 for comparison with the X-ray image).

to edit the DQ extensions of our calibrated images (using Python). Doing so provided a superior cosmic ray removal process than we had started out with. We then changed the `AstroDrizzle` settings so that any pixel that had a cosmic ray hit in both exposures would be set to -9999 so that we could easily identify them for our next step.

Next we used a Python program (part of the `imutils`[4] package created by STScI) that performs Inverse Distance Weighted (IDW) interpolation to fill in the gaps in our image where the information was lost due to cosmic ray strikes. This method uses a weighted (by distance) average of known pixels to interpolate a value for each blank pixel. This served the purpose of giving some approximation of the information that was lost in those pixels.

Once this was done and the WCS coordinates were updated to better match that of our archival radio image, we performed galaxy subtraction as in the F160W case (Figure 2.5). The final image is shown in Figure 2.7.

2.1.2.3 WFPC2 + F791W

Much of the data reduction for this data set was done by a collaborator (Mihai Cara). The data set was initially problematic due to the very noisy background present using the standard data reduction techniques above. Our collaborator experimented with several techniques for improving the image quality when drizzling the frames, with some amount of success, though the graininess in the image remains (Figure 2.7).

[4] `http://www.github.com/spacetelescope/imutils`

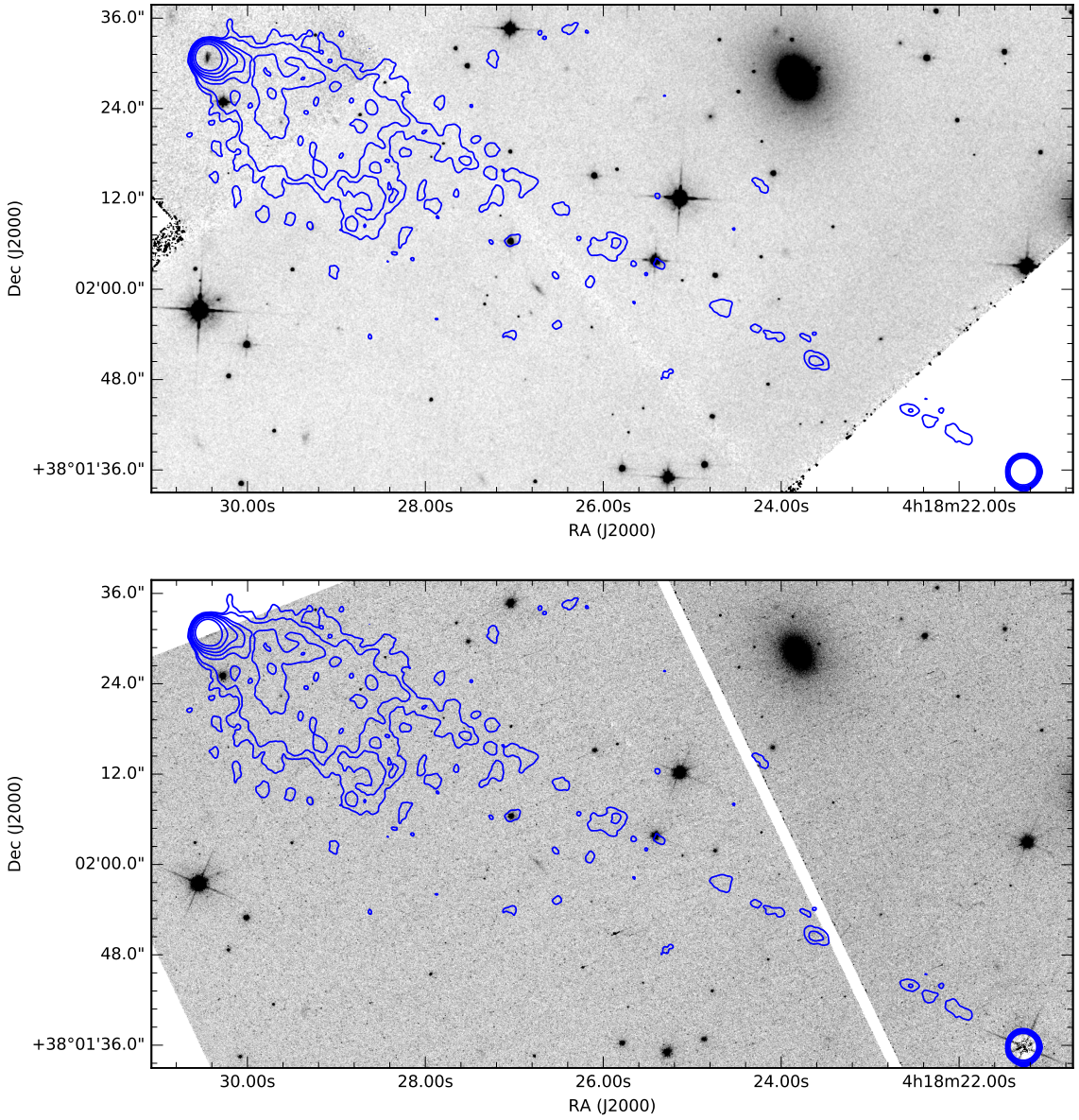

Figure 2.7 The final images for the *HST*/WFPC2+F791W (*top*) and the galaxy-subtracted *HST*/WFC3/UVIS+F850LP (*bottom*) data sets, with radio contours overlaid in blue. Both data sets were ultimately used only to set upper limits on the flux of each jet component in their fields of view (see §3.2).

2.2 X-Ray

In this section our new and archival *Chandra* X-ray Observatory data is discussed as well as the processes that were used to improve the data quality.

2.2.1 Observations

Three sets of *Chandra* data were acquired - one being our own deep observation (Obs ID 14990), another short observation from the Chandra Data Archive (9279), and the third grating observation procured by a collaborator (16219) (Table 2.2). All three data sets were obtained using the Advanced CCD Imaging Spectrometer (ACIS) onboard *Chandra*, in particular using the ACIS-S array of CCDs. The ACIS-S array allows for high resolution X-ray imaging at an energy range of 0.1 to 10 keV, with a field of view of 8.3 x 8.3 arcmin and a pixel scale of 0.492 $\pm$ 0.0001 arcsec/pixel (Chandra team, 2014). The ACIS detector has the capability of generating high-resolution images as well as moderate-resolution spectra, with the option of combining it with either the High Energy Transmission Grating (HETG) or Low Energy Transmission Grating (LETG) to achieve higher resolution spectra, though for our purposes we did not include a grating for our new observation. HETG was used on the 16219 observation, and so we used the "order-zero" image and not the grating data itself. The ACIS detector, like all X-ray detectors, measures individual photons − the large energy of individual photons combined with the relatively small count rate makes this ideal.

The ACIS detector has a section which is exposed for a set time ("full frame time" adjustable from 0.2 to 10 s), after which the charges are quickly read out in parallel into a separate frame. While the next exposure is being taken, the charges are read out from the frame store region serially, at which point any "events" are detected (described further in §2.2.2). To distinguish between good events and bad events (such as cosmic rays), ACIS employs a small "event island" (which is a grid of several pixels) over which the cleaning algorithm is applied. The 14990 and 9279 data sets employ the VFAINT mode of ACIS, which utilizes a 5x5 event island. This is optimal for very faint sources, such as jet knots, as it does a much better job of excluding background events - by a factor of up to 1.4 (Vikhlinin, 2002). The downside to this mode is that for bright

Table 2.2: Relevant information for the *Chandra* data analyzed

test

Obs ID	Exp. Time (ks)	Data Mode	Obs. Date
14990	92.1	VFAINT	01/10/2013
16219	143.41	FAINT	11/04/2014
9279	9.2	VFAINT	12/08/2008

sources where pile-up superimposes events over one another, it can exclude good events. The 16219 data set instead uses the FAINT mode, in which a 3x3 event island is used to detect background events. FAINT mode is preferred when dealing with bright sources.

For the 14990 observation, we used Alternating Exposure mode (also known as Interleaved Mode) which allows for alternating between two different exposure times. We interleaved four frames of 1.5 s with one frame of 0.3 s. This mode is sometimes used when observing a very bright source (such as an AGN) where pile-up is an issue, giving a long-exposure frame that has pile-up and a relatively un-piled short-exposure frame. The short-exposure frame is only used for the region within 10 arcsec of the quasar. The downside to this is that the two exposures are not meant to be merged, but analyzed separately, and so some efficiency is lost.

2.2.2 Data Reduction

The data from *Chandra* was processed using version 4.8.0 of the Chandra Interactive Analysis of Observations (CIAO) software (Fruscione et al., 2006). As mentioned before, X-ray detectors measure individual photons. The list of these detected photons is stored in an "event file," with parameters such as the time of arrival, energy of the photon, position on the detector, etc. Event files are stored in FITS format. The primary data set used was the 14990 data set; the other data sets were used for supplementary purposes as described later.

The data was first reprocessed using the CIAO task `chandra_repro`. This is a script which automates the standard recommended X-ray data processing tasks. Arnaud et al. (2011) provides a thorough description of this processing and how the events are used to make an image. Reprocessing is beneficial because the calibration files are continuously being improved. The end result of this script is to refine the event parameters and create a "level=2 event file," which can be used for data analysis. The primary calculation performed is to determine the "grade" of each event. An event requires that a pixel exceeds a minimum charge threshold. The event is graded by considering the eight adjacent pixels and noting which of those also have a charge that exceeds the minimum threshold. The different grades then determine the "resolution" of each photon impact as well as to filter out particle impacts. The total charge of the event is the sum of the charge of those pixels that were above the minimum threshold; this can then be converted into the event energy by using the response matrix (discussed in §3.3). Another task the script performs is to remove any background flares by analyzing the light curve during the observation window. The script also updates the observation-specific bad pixel file.

The default parameters were used when running the `chandra_repro` task. For ACIS, this means using the Energy-Dependent Subpixel Event Repositioning (EDSER) algorithm (Li et al., 2004). This algorithm uses the fact that the PSF is smaller than the size of the pixels to improve image quality when subsampling (Figure 2.8). This is possible because all *Chandra* observations are dithered − rather than pointing at a fixed position, the telescope is continually dithering in a Lissajous pattern. The other important parameter is that of VFAINT background cleaning. Since we performed our observations in VFAINT mode, we had the option of using the larger (5x5) event island for cleaning the background. This can allow for better flagging of background events by using more pixels when determining the grade of an event. At its best, this can reduce the particle background by a factor of 2 near 0.5 keV and by a factor of 1.1−1.15

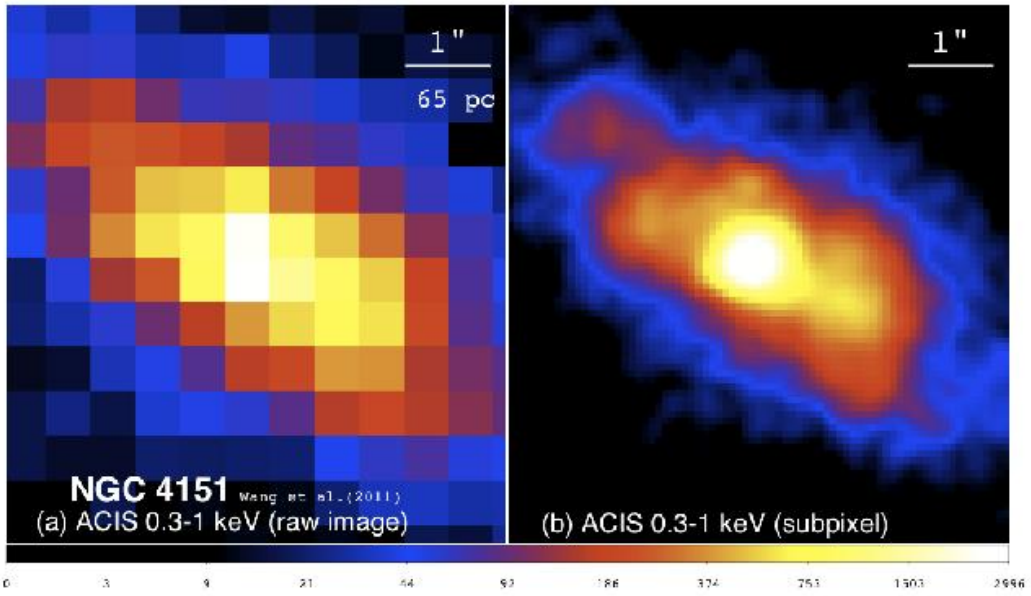

Figure 2.8 The core of NGC 4151 showing the comparison of the raw ACIS image (*left*) and subpixel sampling (1/8 native pixel size) using the EDSER algorithm (*right*). Adapted from Wang et al. (2011).

over the 1−5 keV energy range. However, there is an added risk of real events being excluded. This risk becomes a certainty for bright sources where pile-up is an issue. For our data set, a great many real events were excluded by the VFAINT background cleaning near the AGN core. Given the proximity of several of the jet regions to the core, we opted to not use the VFAINT background cleaning. Overall, the difference it made in the background pixel counts was not large for our chosen energy range (0.5−7 keV).

We used an energy filter of 0.5−7 keV because it is the range least affected by the quantum efficiency (QE) degradation in ACIS over time (Figure 2.9). QE is the fraction of incident photons detected by the CCD. It is thought that the ACIS detectors are being coated with some material(s) over time that decrease the QE (Chandra team, 2015). CIAO applies a correction for the modeled effect of QE with energy.

The final image for the 14990 data set contains a bright readout streak across the

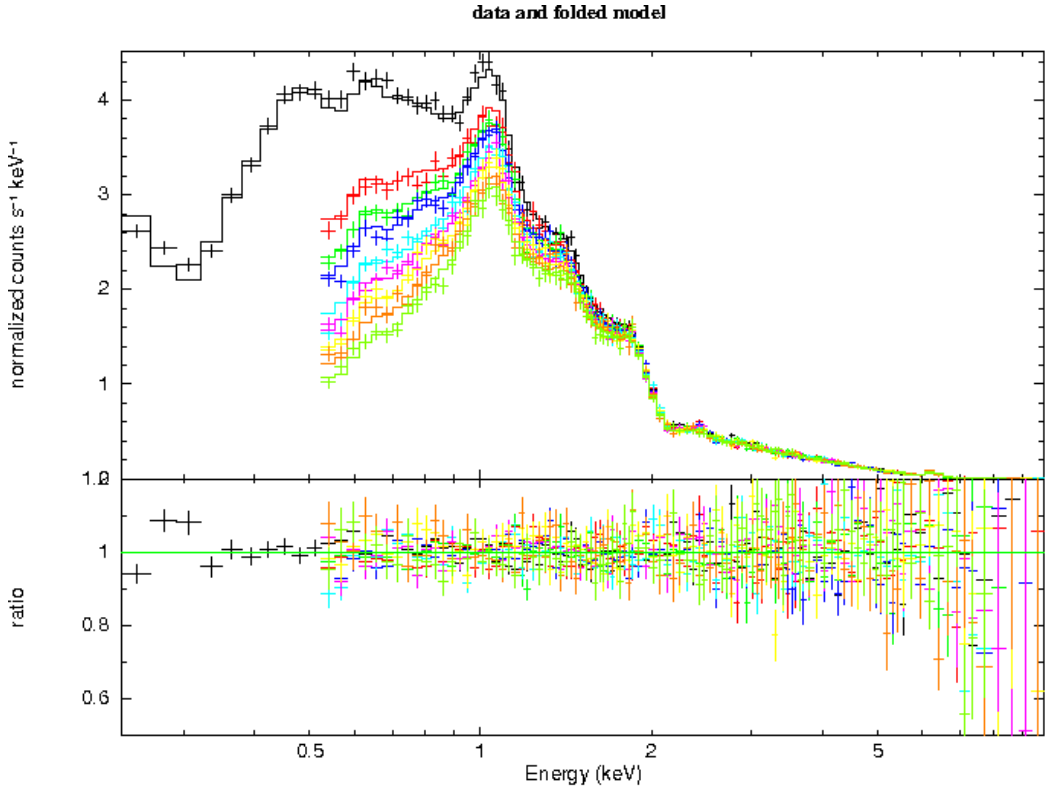

Figure 2.9 Fitted spectra from observations of A1759 (in 2000, 2002, 2004, 2005, 2009, 2010, 2011,2012 and 2013) showing the energy-dependent decrease in QE for the ACIS-S detector with time. From `http://cxc.harvard.edu/ciao/why/acisqecontam.html`.

AGN core. This is due to the way in which ACIS continues to take data even as it reads out a frame. This streak can be removed, however for our data set it did not pose any issues and so we left it in. The readout streak in the 16219 image, however, overlapped some of the jet components close to the core. This, combined with its relatively low flux due to being an HETG observation led us to not combine it with our primary image.

Once the level=2 event file is made, astrometry correction can be performed. This was important for our data because there was a significant offset from that of the radio image. The CIAO tasks `wavdetect`, `wcs_match`, and `wcs_update` were used for this purpose. `wavdetect` is a task that statistically detects sources in the image. This was problematic for our data set because the field had only two bright X-ray sources present

and one whose centroid was not well-constrained due to its faintness. `wcs_match` is used to match the astrometry of detected X-ray sources with those in an external catalog, preferably one that has very good astrometry. Given our particular field and the fact that `wcs_match` requires at least three detected sources to align to, the only option available to us was to use the Two Micron All Sky Survey (2MASS) catalog. The astrometry of the 2MASS catalog is ± 0.1 arcsec, a significant improvement over the *Chandra* absolute astrometry accuracy of ± 0.5 arcsec (Weisskopf et al., 2003). Due in part to the few sources available for matching, we excluded rotational corrections from being made. `wcs_update` was then used to apply the astrometry correction to the event file. The end result showed a significant improvement in the astrometry over the uncorrected image, despite the centroid of the third source not being very precise. The 9279 data set, due to its significantly shorter exposure time, only had two detectable sources and thus was not able to be aligned to any external catalog. For this reason, we did not combine it with our 14990 data set for either the imaging or the spectroscopy.

The images for the 14990 and 16219 data sets were combined and smoothed (Figure 2.10). The combined image is used for visual presentation and not for any photometric or spectroscopic analysis.

The last step of our X-ray data reduction was to create the source and background spectra for each of our jet regions (shown in Figure 2.10). Each jet knot source region was aligned to the WCS coordinates of the *Chandra* image for each of our bands. The naming scheme is that of the letter "K" followed by the approximate distance (in arcsec) from the core to the position of peak flux (e.g., K30's peak flux is ~ 30 arcsec from the center of the AGN core). Background aperture regions were chosen adjacent to each source region to account for the flux due to the AGN. For the source regions that were particularly close to the core, an annulus region was used for the background. The spectra were extracted from these regions using the CIAO task `specextract`. This task

generates the Response Matrix Files (RMFs) and Ancillary Response Files (ARFs) for each source and background region, which are used in converting the charge present in the pixels to the energy. We altered the correctpsf parameter to apply aperture correction to the source regions (aperture correction is described further in §3.2). The energy range was set to 0.5−7 keV with an energy bin of 0.01 keV. The analysis of the extracted spectra is discussed in §3.3. K30, K61, and the northern hotspot (NHS) were the only jet regions with a sufficient number of counts to extract spectra from.

2.3 Radio

We used archival Very Large Array (VLA) imaging for comparison with that of our new *HST* and *Chandra* observations. The radio image used is that from Leahy et al. (1997), shown in Figure 2.11. The observations were done in 1989 with two pointings of the VLA in configurations A, B, C, and D at 8.235 and 8.465 GHz.

We did not perform the data reduction of the archival VLA data set, as the final image was already in-hand.

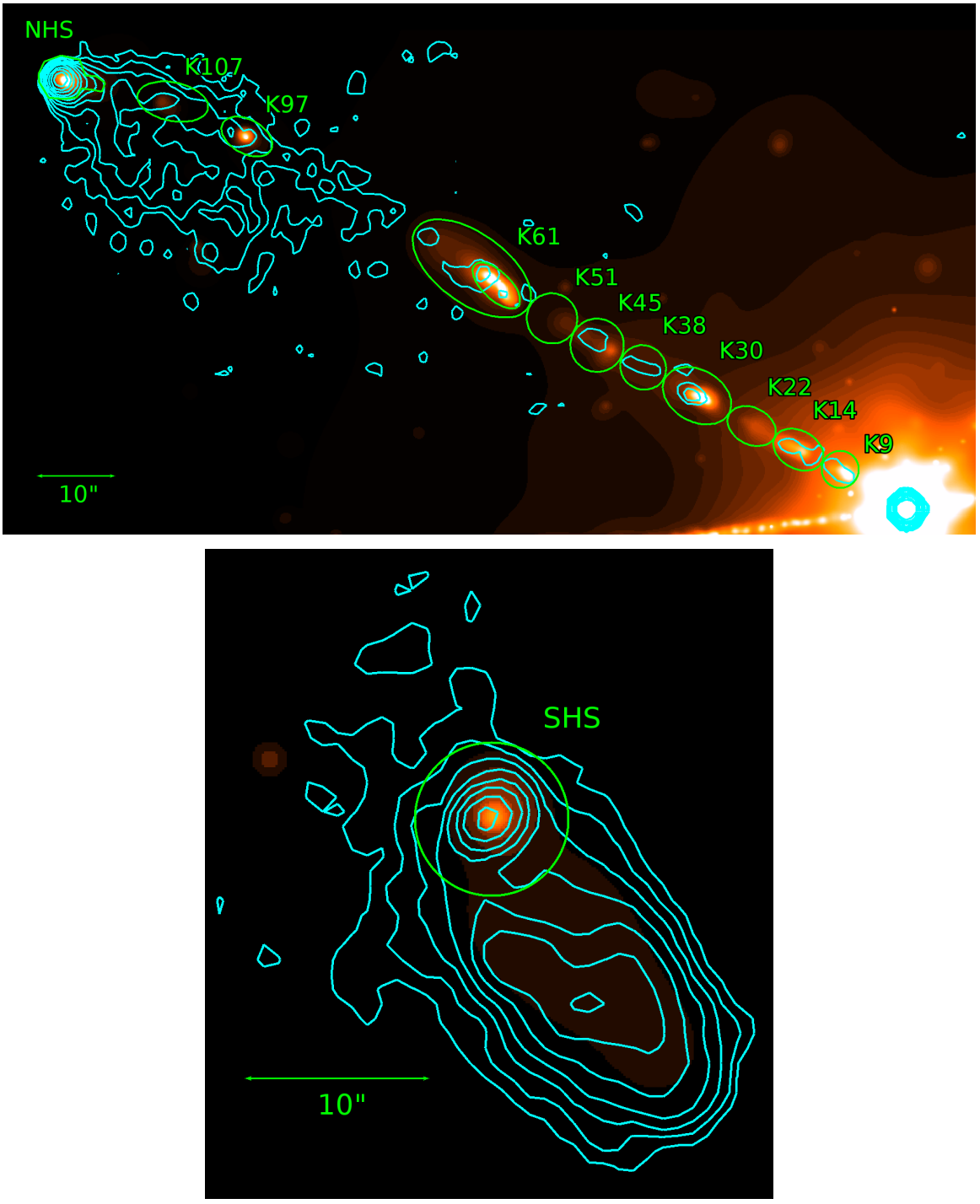

Figure 2.10 Deep *Chandra* X-ray observation of 3C 111 displayed with a heat scale with radio emission overlaid as cyan contours. The *Chandra* image shows emission from eight approaching jet regions (named in green) and the northern hotspot (NHS) (*top*), as well as the southern hotspot (SHS) (*bottom*). Also shown in green are the flux extraction regions for each knot region. Note that significant differences exist between the morphology seen in the two bands.

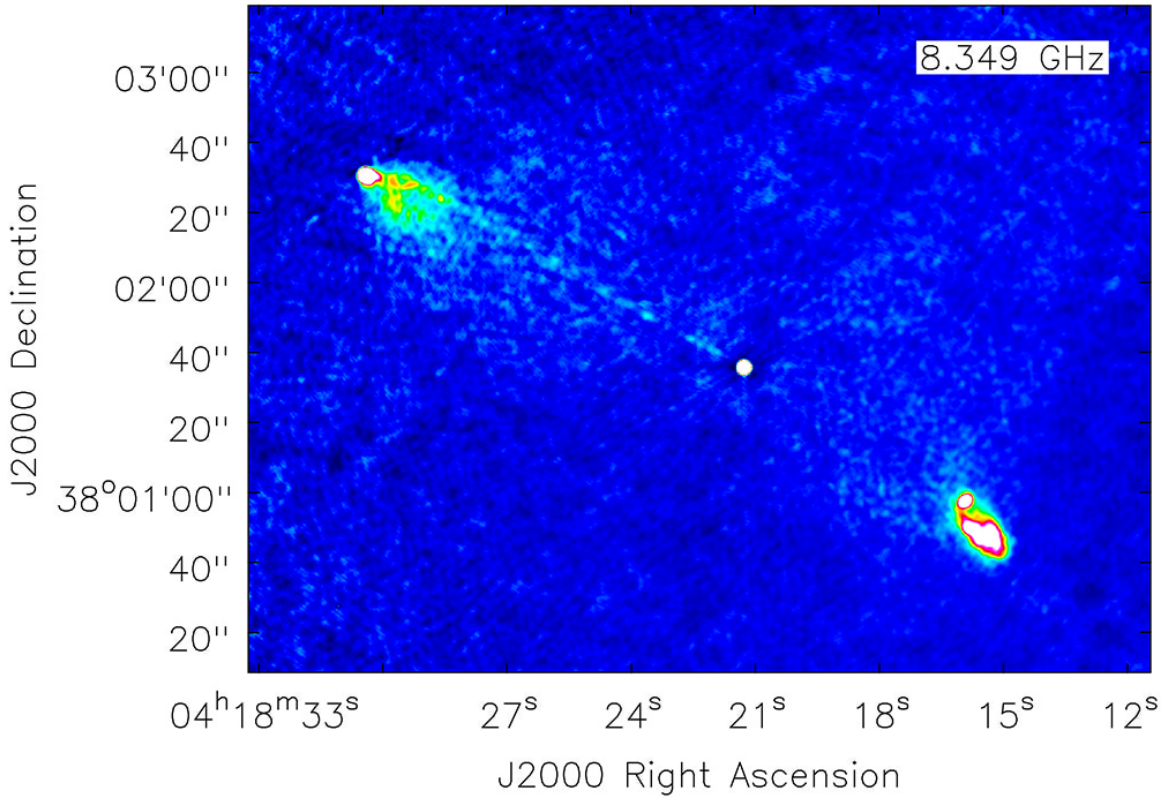

Figure 2.11 Archival VLA image of multiple observations and pointings of 3C 111 at 8.35 GHz (Leahy et al., 1997).

Chapter 3

Data Analysis

3.1 Jet Morphology

The 3C 111 jet can be seen across the electromagnetic spectrum, from the radio through the X-rays. In Figure 2.10, we show our deep *Chandra* imaging of 3C 111, along with archival VLA imaging (Leahy et al., 1997). X-ray emission is evident in at least 8 jet regions, plus the northern and southern hotspot. This emission is also seen in the near-IR, as shown in Figure 2.6, which shows close-ups of four jet regions in the F160W image, respectively the northern hotspot (NHS), outer jet, inner jet, and southern hotspot (SHS). The near-IR image shows emission from most, but not all X-ray emitting jet regions. In the F850LP and F791W images (Figure 2.7), the only jet-related emission that can be seen comes from the northern hotspot. This is likely a result of the high Galactic extinction toward 3C 111 at these wavelengths. Overlaying contours and taking the centroids (peak flux maxima) allows us to compare the morphology in different bands. To aid in this comparison, we named the northern (approaching) jet features using the distance in arcseconds from the nucleus (e.g., knot K14 has its flux maximum $\sim$14 arcsec from the nucleus).

There is significant evidence of differences between the radio, near-IR, and X-ray morphology, as seen in Figures 2.6 and 2.10, as well as in Figure 3.1, which shows the profile of relative flux (each normalized to 1 at an arbitrary point) along the jet in the *Chandra*, F160W, and VLA images. The images were aligned to the radio as described in Chapter 2; we estimate the 1σ errors in the positions from the radio to be < 0.02 arcsec for *HST*, while those in the X-ray image are ± 0.16 arcsec relative to the radio frame of reference according to Rots & Budavári (2011), although to be conservative for this purpose we used ± 0.3 arcsec.

Note that components within $\sim$20 arcsec of the nucleus have flux profiles in the X-ray that are mixed with that of the unresolved nuclear source due to the *Chandra* PSF, and are somewhat piled up in the long frame time, undispersed *Chandra* image. Within $10''-15''$, the knots also lie within the galaxy seen in the near-IR image; though the galaxy has been subtracted, the systematic errors present are larger than for knots further away from the nucleus. Knot K9's X-ray morphology has a strong peak toward its upstream end that is not seen in the radio. Unfortunately, however, it lies too close to the diffraction spike in the F160W image to fully characterize in the near-IR. Knot K14 appears to peak slightly closer to the nucleus in the radio image than in either the near-IR or X-rays. X-ray emission is clearly seen downstream of that component extending nearly continuously to knot K30. That emission is not seen in either the near-IR or the radio (the near-IR emission that is present is more likely due to subtle galaxy features in the same region). That X-ray emission includes a knot seen only in the X-rays, knot K22.

Knot K30, seen in all three bands, has an X-ray flux peak that is located significantly upstream of either the radio or near-IR peaks, with the near-IR peak located closer to the nucleus than the radio one (Figure 3.2). The X-ray flux from K30 also declines much more quickly with increasing distance from the nucleus than in either the

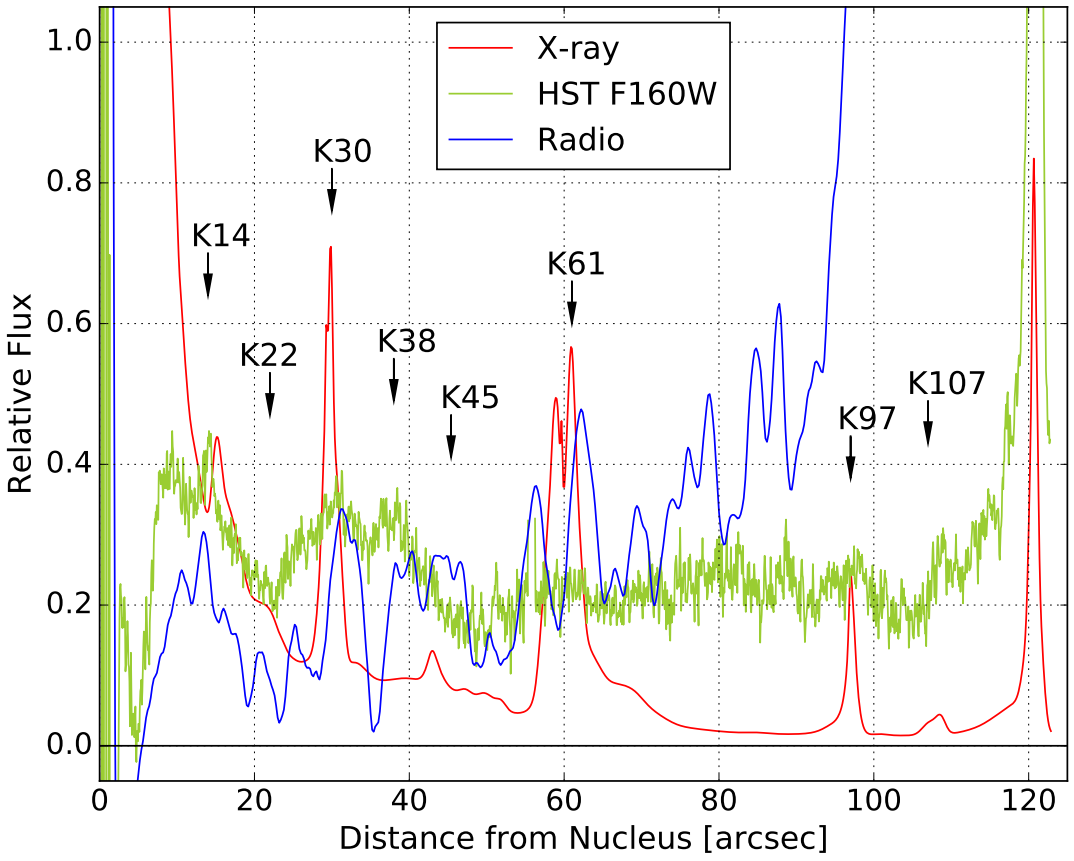

Figure 3.1 Relative flux as a function of distance from the nucleus for the approaching jet of 3C 111, as seen in the radio (VLA image, blue trace), near-IR (*HST*/WFC3/IR+F160W image, green trace) and X-rays (smoothed *Chandra* image, red trace). Each of the three traces was extracted from a slice 1.476 arcsec wide, along a vector extending from the nucleus of the galaxy through the NHS. Exclude regions were used to mask the emission from obvious non-jet sources in the near-IR image. Major knot regions are labeled above the traces.

near-IR or radio, which show similar decline rates (Figure 3.1). The K38−K45 region is also complex. The radio flux of K38 displays two peaks, with the near-IR peak associated with the one closer to the nucleus. The X-ray emission, however, does not peak until ∼42″ from the nucleus, where there is an apparent radio minimum. The radio emission picks up again between 43″ and 45″, while through that region and extending

out to nearly 50″, the X-ray emission appears roughly continuous. Moving further out, there is a flux maximum at about 55″ from the nucleus in the radio image that is not seen in the X-ray or F160W images − the radio peaks appear on either end of the intense X-ray flux at K61. Knot K61, which represents an apparent "kink" in the jet, is seen in both the radio and X-rays. Its X-ray morphology has a "corkscrew" like appearance that is not prominent in the radio, where only its downstream half can be seen. In the optical/near-IR, K61 unfortunately lies very near a bright foreground star and so while there is possible emission in the near-IR it lies too close to the star and its diffraction spikes to have confidence in its detection and/or its flux measurement.

Four emission components are seen within the extended lobes. Within the northern lobe we see knots K97 and K107, as well as the flux maximum of the NHS itself. While these three components have outwardly similar morphologies in the X-ray, near-IR and radio, close examination reveals important differences. In particular, it is only in the radio that one appreciates the extent of the northern lobe, which extends for over 30 arcsec in a "plume" shape that includes both K97 and K107. In the X-ray and near-IR, we see only the three components (with K97 barely detected), plus extensions to the NHS in two directions, the first being back upstream pointing at K107, and the second one pointing off to the southwest, parallel to the flux contours defining the lobe's southern edge. The latter could indicate material outflowing from the hotspot, similar to what has been postulated for the 3C 273 jet by Roeser et al. (1996), while the general shape of the jet in that region indicates that the jet does bend as it enters the lobe. A close look at the NHS itself also reveals that its flux maximum is not located at the same position in the radio, near-IR, and X-ray − the X-ray maximum is seen upstream of the maxima in the near-IR and radio (which are aligned with each other). This misalignment, which is suggestive but not firm at the 2.5−3 σ significance level, is shown in Figures 2.6 and 2.10, and quantified in Figure 3.2.

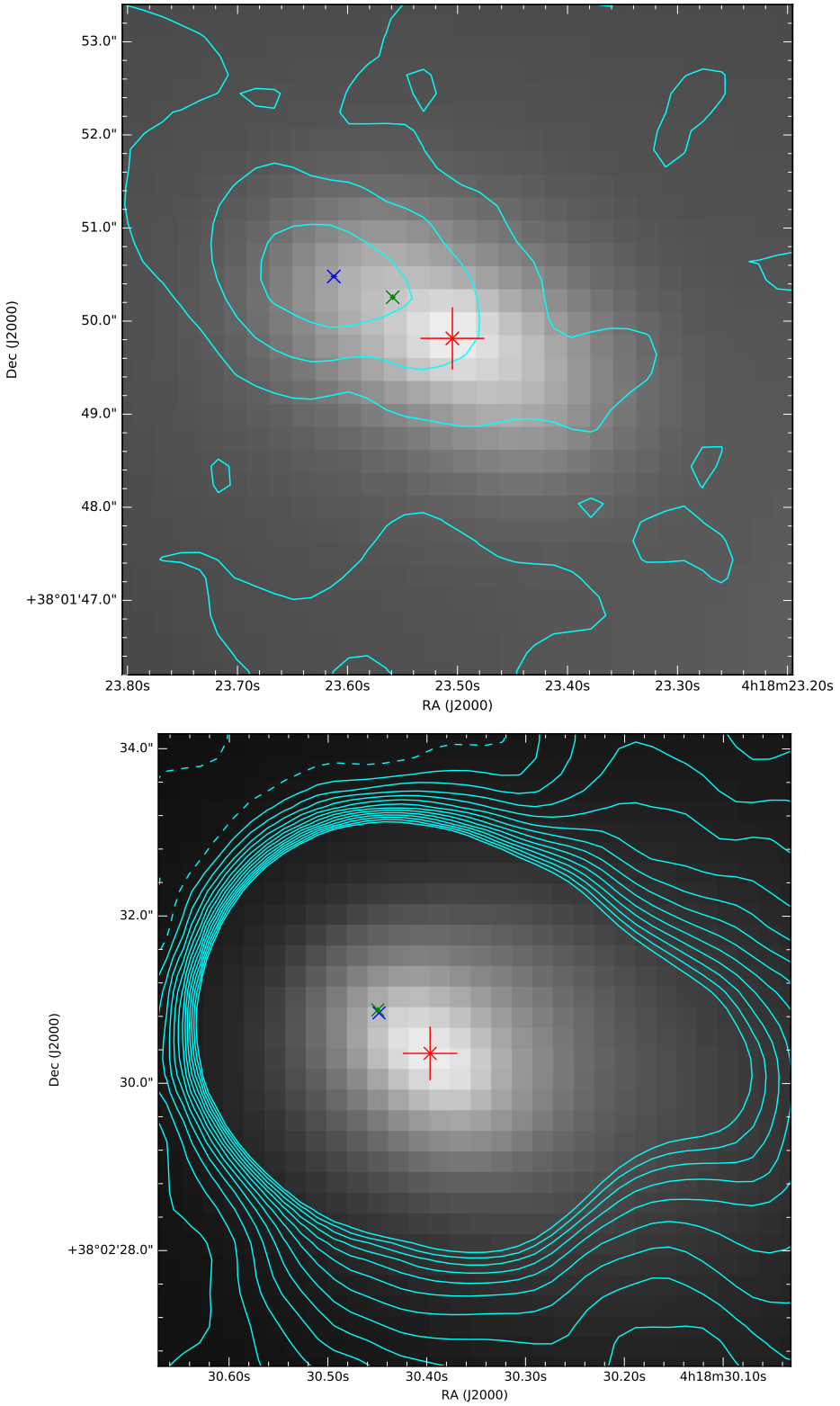

Figure 3.2 Close-up views of the K30 (top) and NHS (bottom) regions of the *Chandra* image, showing the location of the flux maxima in the radio (blue), near-IR (green), and X-ray (red) bands. The sizes of the error bars on each position are shown. Radio contours overlaid in cyan.

In addition, we also see for the first time X-ray and near-IR emission from the SHS. The radio and near-IR emission from the SHS flux are well aligned (Figure 2.6), while there simply are not enough photons detected in the *Chandra* image to accurately compare its flux maximum position, as only 32 ± 8 counts are seen from the SHS and the X-ray emission is significantly extended.

We hope to compare the morphology between bands in the manner of Figure 3.2 for other emission components in future work (see §4.4).

3.2 Photometry

This section describes the methods and tools used to determine the flux in each jet region, which differ considerably between near-IR/Optical/UV (*HST*), X-ray (*Chandra*), and radio (archival VLA).

3.2.1 Near-IR/Optical/UV

The technique of aperture photometry was used to determine the flux in each of the jet regions (shown in Figure 2.10). Aperture photometry is a simple method of determining the counts (and therefore flux) in a source region wherein the number of observed counts in each pixel of a source region are summed up and the background sky contribution is removed. For each source region, background regions were chosen nearby to estimate the local source background. Determining the best size of the source region is an issue because a larger source size means more pixels from which the error contribution increases, leading to a smaller signal-to-noise ratio (SNR). Since we dealt with extended emission rather than point sources, we determined the size of the source regions by comparing the knot sizes in the smoothed *Chandra* image shown in Figure 2.10 with

those in the near-IR and radio bands (Figures 2.6 and 2.11), as the observed size of jet knots can vary with wavelength.

However, the PSF from the source will be larger than the region used, meaning that some small amount of source flux is not being accounted for. The technique of aperture correction is used to account for this missing flux without adding in the noise from all the additional pixels outside the source region. In practice this is generally done using aperture growth curves (Howell, 1989). At the time we performed the *HST* photometry, such aperture growth charts had not been made for the WFC3 instrument. To determine the amount of aperture correction, we modeled a PSF at the source position for each of our original non-mosaicked images and then combined them using the same procedure as we did for the main image. Each PSF model was made using the TinyTim program[1] (Krist et al., 2011); though it can model the PSF of the WFC3 instrument, it is not fully supported and is known to suffer from various issues (Biretta, 2012, 2014). We then took the ratio of the enclosed number of counts vs the total counts in the mosaicked PSF to determine the aperture correction factor. For K9, which is a circle of radius $\sim$2.4 arcsec, this lead to an aperture correction factor of 1.023 in the near-IR (i.e., that $\sim$2.3% of the flux was not enclosed in the source aperture prior to applying aperture correction).

At the time of this writing, aperture growth curves have since been published for WFC3[2]. The growth chart shows that a 2 arcsec aperture for WFC3/IR+F160W will enclose $\sim$97% of the source flux giving an aperture correction factor of $\sim$1.031. Given our use of a larger aperture, the method we used seems in good agreement with the published growth chart. The other source regions we used were larger than that of K30 and thus had smaller aperture correction factors. Note that both aperture correction methods are determined using point sources and so most likely represent

[1] `http://www.stsci.edu/hst/observatory/focus/TinyTim/`
[2] `http://www.stsci.edu/hst/wfc3/phot_zp_lbn`

slight overestimates of the flux missing from the source region in the case of extended emission. We applied aperture correction for WFC3/IR+F160W and WFPC2+F791W, however for WFC3/UVIS+F850LP we were unable to properly model the mosaicked PSFs. However, since we only used the F850LP image to establish upper limits on the source fluxes, combined with the fact that the aperture correction factors are even smaller than those for WFC3/IR, the lack of aperture correction is not significant.

Exclude regions were used to omit the counts from stars, galaxies and diffraction spikes in all source and background regions. Local background regions were chosen such that they contained a larger number of pixels than the source region where possible.

For all three of our mosaicked/drizzled *HST* images, the pixels had units of counts per second (count rate). This was done because, after drizzling and mosaicking, each pixel has a different effective exposure time. A Python script of our making was used to determine the background-subtracted count rate in each source region, which can then be converted into flux. The `pyregion` package and a custom script (created by Mihai Cara) were used to convert the source, background, and exclude regions into pixel masks which could then be imported into `NumPy` arrays in Python using the `astropy` package (Astropy Collaboration et al., 2013). Sigma clipping was applied to the background pixel arrays to remove any outlier pixels that were missed by the exclude regions. Since galaxy subtraction was applied previously, some of the pixels had negative count rates, which obviously is not realistic. To rectify this, in source/background regions where there were negative pixel values, we subtracted the minimum pixel value so that the minimum value would then become 0. This had no effect on the background-subtracted count rate, but does affect the error. This is necessary because in some cases the total background counts could be negative, which is troublesome given that the CCD error equation involves taking the square root (due to Poisson statistics). From testing with

sample arrays, this seemed the best method to determine the error for the galaxy-subtracted source regions. The issue of negative pixels is unavoidable when doing any sort of global sky subtraction, such as that performed by default by `AstroDrizzle`, though there appears to be no standardized method to deal with it. In any case, the errors are small for the F160W image.

The average count rate per pixel in the background region was determined by

$$\overline{DN}_{\rm sky} = \frac{DN_{\rm sky}}{n_{\rm B}}, \tag{3.1}$$

where $DN_{\rm sky}$ is the total number of counts per second ("data numbers") in the background region and $n_{\rm B}$ is the number of pixels in the background region. The total number of background-subtracted counts per second in a source region was then determined by

$$DN_* = \sum_{i=1}^{n_{\rm pix}} \left(DN_{\rm source,i} - \overline{DN}_{\rm sky} \right), \tag{3.2}$$

where $DN_{\rm source,i}$ is the count rate of a given pixel in the source region and $n_{\rm pix}$ is the number of pixels in the source region.

The background-subtracted count rate can then be converted into flux by

$$F_* = DN_* \cdot PHOTFLAM \cdot PHOTPLAM \quad [\text{erg s}^{-1}\ \text{cm}^{-2}], \tag{3.3}$$

where PHOTFLAM and PHOTPLAM are photometric calibration values found in the header of the drizzled image. F_* is then multiplied by the aperture correction factor for the source region to get the total flux. This must then be corrected for extinction using

$$A_\nu = -2.5 \log_{10} \left(\frac{F_*}{F} \right) \tag{3.4}$$

(e.g., Schneider 2006), where A_ν is the wavelength-dependent extinction coefficient, F_*

Table 3.1. Jet Component Flux Densities

Region	Radio (mJy)	F160W (μJy)	F850LP (μJy)	F791W (μJy)	2 keV (nJy)
K9	6.91 ± 0.30	4.88 ± 0.12	$< 8^a$	...[b]	1.07 ± 0.20
K14	9.35 ± 0.44	5.38 ± 0.15	$< 10^a$	...[b]	0.91 ± 0.16
K22	3.78 ± 0.42	0.46 ± 0.20	$< 11^a$	...[b]	0.40 ± 0.11
K30	13.15 ± 0.60	8.75 ± 0.23	...[c]	$< 11^a$	2.26 ± 0.26
K40	8.25 ± 0.44	2.13 ± 0.20	$< 14^a$	$< 7^a$	0.35 ± 0.09
K45	11.96 ± 0.52	1.13 ± 0.25	$< 17^a$	$< 9^a$	0.55 ± 0.11
K51	6.03 ± 0.49	1.72 ± 0.18	$< 16^a$	$< 8^a$	0.22 ± 0.08
K61	38.13 ± 0.95	1.77 ± 0.46^d	$< 22^{a,d}$	$< 23^{a,d}$	4.38 ± 0.40
K97	27.88 ± 0.42	2.01 ± 0.28	$< 11^a$	$< 6^a$	0.59 ± 0.09
K107	58.00 ± 0.51	4.70 ± 0.36	$< 16^a$	$< 12^a$	0.18 ± 0.06
NHS	610.31 ± 0.47	121.0 ± 0.6	...[c]	44.3 ± 4.0	1.86 ± 0.21
SHS	182.52 ± 0.63	13.39 ± 0.53	$< 22^a$	...[b]	0.35 ± 0.09

[a]Flux quoted is a 2σ upper limit.

[b]Knot is off chip.

[c]At chip border, significant part of region off chip.

[d]Bright star plus diffraction spikes within region.

is the observed flux, and F is the extinction-corrected source flux. The extinction coefficients were taken from the NASA/IPAC Extragalactic Database (NED)[3]. The values used were 0.846 for F160W, 1.996 for F850LP, and 2.560 for F791W. The resulting flux density values for each source region are given in Table 3.1.

To estimate the error in count rate (DN), first the count rate needed to be converted into counts. This was done by multiplying the pixel DN value by its associated weight map pixel[4] (in the WHT extension of the drizzled image), the value of which is the calculated exposure time of that pixel. The uncertainty in source counts were then

[3]`http://ned.ipac.caltech.edu`

[4]`http://documents.stsci.edu/hst/HST_overview/documents/DrizzlePac/ch43.html#610049`

determined for each source region using

$$\sigma_{\mathrm{N}_*} = \sqrt{N_* + n_{\mathrm{pix}} \left(1 + \frac{n_{\mathrm{pix}}}{n_{\mathrm{B}}}\right) (N_{\mathrm{sky}} + N_{\mathrm{D}} + N_{\mathrm{R}}^2)} \tag{3.5}$$

(e.g., Howell 2006), where N_* is the total number of background-subtracted counts in the source region, N_{sky}, N_{D} and N_{R} are the total number of counts (or electrons) per pixel in the background, due to dark current, and due to read noise, respectively. The $(1 + n_{\mathrm{pix}}/n_{\mathrm{B}})$ term attempts to account for the noise introduced due to the relative size of the chosen background region. The median dark current was found in Rajan et al. (2010) and in the dark frame that corresponds to each image, while the average read noise was contained in the header; both were corrected for the smaller (drizzled) pixel size. The various chips in WFPC2 have differing values for read noise and dark current which were used for the relevant jet regions.

The error in source counts was then divided by the median exposure time per pixel in the source region to get the total error in source count rate. This was then converted into the error in flux as described above.

3.2.2 X-Ray

Spectra were fitted to the observed X-ray data for each source region to determine the flux. This is discussed in §3.3.

3.2.3 Radio

To determine the source flux in each source region of the radio image, we used the Common Astronomy Software Applications (CASA) package (McMullin et al., 2007), developed in part by the National Radio Astronomical Observatory (NRAO) for use on

radio data. The radio image was imported to CASA and the `imstat` function was used to determine the flux in each source region. A global background region was chosen to estimate the RMS noise ($\sigma_{\rm sky}$). Each pixel in the radio image has units of Jy/beam. The sum of each pixel in a source region can then be divided by the area of the clean beam to give the flux density of the region (in Jy). The area of the clean beam is determined by

$$A_{\rm b} = \frac{\pi\theta^2}{4\ln 2} \tag{3.6}$$

(e.g., Condon 2015), where $\theta^2 = B_{\rm min} \cdot B_{\rm max}$, the product of the major and minor axes of the clean beam (in pixels). The size of the clean beam was determined when the image was originally created. The radio flux density of each jet region is given in Table 3.1.

Unlike the case with *HST*, radio observations do not measure photon "counts", and so counting (Poisson) statistics are not used to determine the error. Instead, the error is Gaussian in nature. The error in flux density is given by

$$\sigma_{F_\nu} = \sigma_{\rm sky}\sqrt{\frac{n_{\rm pix}}{A_{\rm b}}}, \tag{3.7}$$

where $n_{\rm pix}/A_{\rm b}$ is the number of clean beams in the integration area of the source region.

3.3 X-Ray Spectroscopy

As discussed in §2.2.2, the `specextract` function in CIAO was used to extract spectra for the K30, K61, and NHS regions and their associated background regions. The *Sherpa* software package (Freeman et al., 2001) was used to fit models to our observed spectra. We used *XSpec* models contained in *Sherpa* to do the fits, namely *xspowerlaw* and *xsphabs*, which respectively model a photon power law fit and background photoelectric absorption. The CSTAT statistic was chosen as our maximum likelihood

function to assess the goodness of fit, along with the Simplex (aka Nelder−Mead) fitting optimization method. The CSTAT statistic is equivalent to the Cash statistic (Cash, 1979), a Poisson likelihood function, but allows for easier checking of the goodness-of-fit. Source and background spectra were modeled independently, as is required by the CSTAT statistic. Fits were done on unbinned data per the recommendation of Arnaud et al. (2011), over the 0.5−7 keV energy range.

We used a value of $N_{\rm H} = 8.6 \times 10^{21}$ cm^{-2} for the absorption column density. This value was obtained using the *Chandra* HETG data by our collaborator Francesco Tombesi (Tombesi et al. 2016, in preparation). The other *Chandra* data sets at our disposal suffer from pile-up in the nucleus and thus cannot be used to accurately determine the value of $N_{\rm H}$.

The goodness-of-fit of each model was checked in two ways: first, by looking at the reduced statistic; and second, by running a simulation of the model and using the `plot_cdf` function to check that the cumulative distribution function had a median at about 0.5[5]. The *xspowerlaw* model is of the power law

$$F_{\rm E} = KE^{-\Gamma}, \tag{3.8}$$

where E is the energy, Γ is the photon index and K is the normalization constant. The photon index Γ is related to the spectral index α such that $\alpha = \Gamma - 1$, where $F_\nu \propto \nu^{-\alpha}$ (Peterson, 1997). The fitted spectral parameters for each source region are given in Table 3.2. Errors in spectral index and normalization are given at 90% confidence intervals. The three fitted jet regions have spectral indices between $\alpha = 0.76$ and $\alpha = 1.01$.

The flux was determined using the `calc_energy_flux` function over a range of 0.5−7 keV; the flux density was determined at 2 keV. Simulations were used to determine

[5] `http://pysherpa.blogspot.com/2012/06/goodness-of-fit-with-cstatcash.html`

Table 3.2. Jet Component X-Ray Spectra

Region	Normalization (erg s^{-1} cm^{-2})	α	χ^2_ν
K30	$(4.27 \pm 0.58) \times 10^{-14}$	0.76 ± 0.29	0.944
K61	$(8.28 \pm 0.82) \times 10^{-14}$	1.01 ± 0.21	0.985
NHS	$(3.49 \pm 0.48) \times 10^{-14}$	0.83 ± 0.28	0.927

the errors at 68% confidence intervals. The fitted spectral parameters were used for the three jet regions with sufficient counts; for all other jet regions, the average of the three fitted spectral indices ($\bar{\alpha} \approx 0.87$) was used. The flux density values for each jet source region are given in Table 3.1.

Chapter 4

Results & Discussion

4.1 Jet Spectral Energy Distribution

We have extracted fluxes (as described in §3.2) and created spectral energy distributions (SEDs) for all jet and hotspot regions. The extraction regions used are shown in green in Figure 2.10. The flux densities are given in Table 3.1.

The resulting SEDs for all components are shown in Figure 4.1. Figure 4.1 also includes ground-based K and R-band fluxes for the NHS that were previously published in Meisenheimer et al. (1997), corrected with updated values for the Galactic extinction (squares in the lower right panel), as well as a 1.3 mm flux from IRAM (Meisenheimer et al., 1989). The 1.3 mm IRAM point lies very close to the power law ($\alpha_{\rm R} = 0.85$) extrapolated from the 8.4 GHz observation of Leahy et al. (1997). The apparent discrepancy between our F160W flux and the extrapolation of the K-to-R band spectral index from Meisenheimer et al. (1997) merits further discussion. We chose a slightly larger aperture than Meisenheimer et al. (1997), to include faint extended flux not seen by those authors. This is only 3% of the total, and both after and before this, our F791W flux is within 1σ of the Meisenheimer et al. (1997) K-to-R band extrapolation.

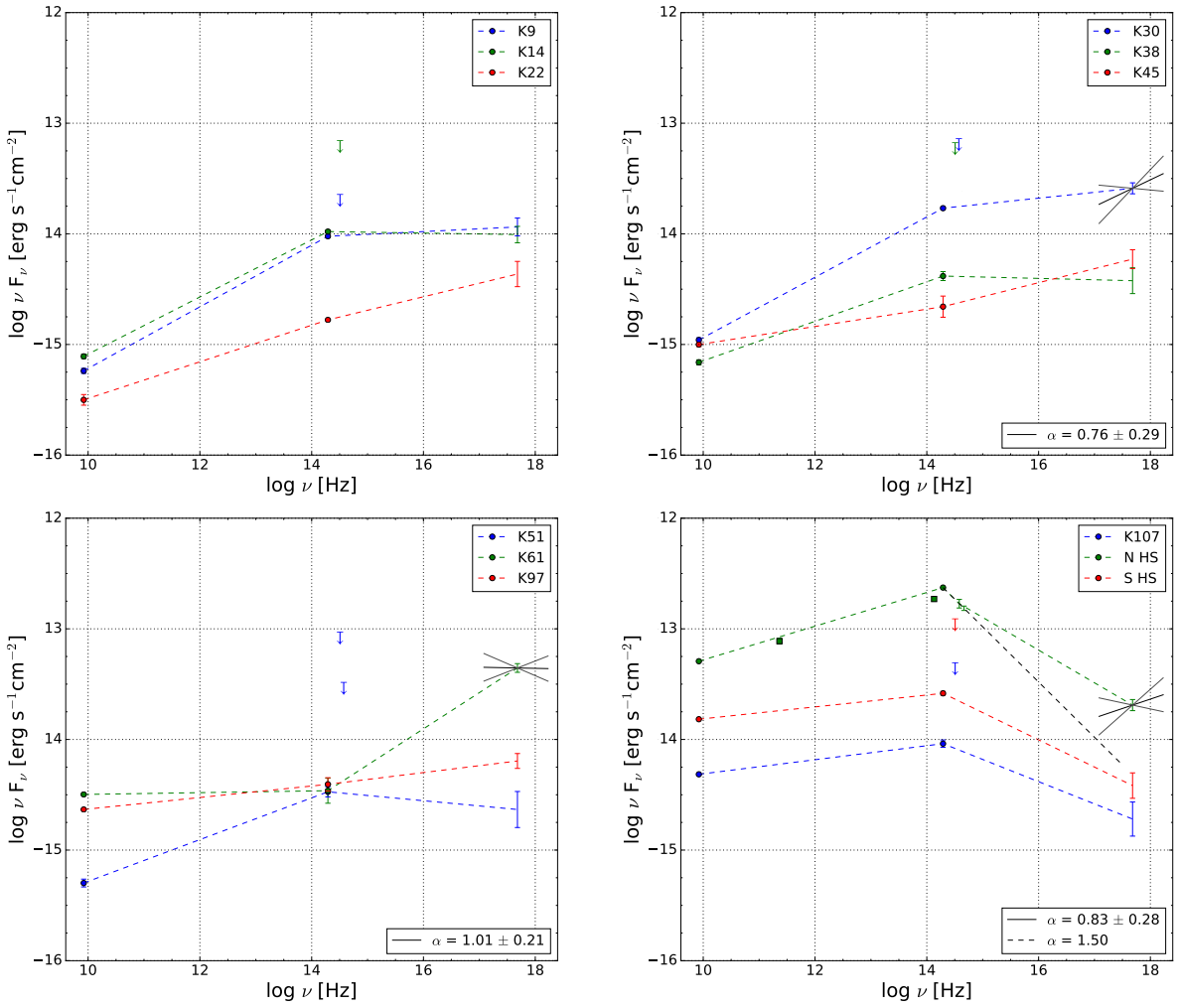

Figure 4.1 SEDs for the jet and hotspot regions. We have connected all detected fluxes by simple power laws (dashed straight lines in these log−log plots). Where X-ray spectra are fit, these fits are indicated with "butterflies" of 90% confidence and the spectral slope values are given at bottom right. In the NHS, we also plot as the black dotted line the observed near-IR−to−Optical spectral index.

While it is possible that our flux in F160W is incorrect, we consider this unlikely given our careful choice of a source-free background region and the well-established nature of the *HST* flux scale. Alternatively, the K-band flux measurement of Meisenheimer et al. (1997) was affected by either poor background subtraction or poor flux calibration. We favor this explanation, as due to the crowded field (shown in Figure 2.6) it is likely that the background region in a ground-based image, like that of Meisenheimer et al. (1997),

would include flux from one or more neighboring objects, thus causing an apparent underestimate of the source flux.

As can be seen, most of the jet components have diverse SED shapes that naively can be fit by synchrotron emission from a single electron population. For example, knots K45 and K97 appear to be fit reasonably well by single power laws extending up to X-ray energies, and most other knots have an X-ray flux that is significantly below the extrapolation of the radio−to−near-IR power law. However, we do not favor this simple interpretation, as in the NHS the fitted X-ray spectral slope is much harder than the extrapolation of the radio-to-optical synchrotron component, while in knot K61 the X-ray flux is a factor of about 4 higher than a simple extrapolation of the radio−to−near-IR power law. Thus a second emission component is necessary to fit the SED of these jet knots and possibly others. In broad terms, such a spectral shape has been seen before in other quasar jets (e.g., PKS 0637-752, knots WK7.8 and WK8.7, Mehta et al., 2009), and requires either a contribution from another, inverse-Compton mechanism (the so-called EC/CMB mechanism, described in §1.6.2), or alternately a second, entirely distinct high-energy electron population to account for the X-ray emission. Here, however, the fitted X-ray spectra combined with the fact that the X-ray emission of knot K30 and the NHS has a flux maximum at a different location than the near-IR or optical emission, makes the two-component synchrotron interpretation much more likely. Additionally, a Doppler factor of $\delta \gtrsim 45$ is required to explain the observed properties of the NHS flux if EC/CMB is the dominant emission mechanism at work (see §4.3).

4.2 Jet Deceleration

The jet of 3C 111 is unique for several reasons. Chief among these are the fact that both the approaching and receding hotspots can be seen in all bands, and its extreme length,

with X-ray and near-IR components seen in the jet for more than 100 arcsec. The data we present here can be used to place a variety of constraints on both the kinematics of the jet as well as the X-ray emission mechanism. Here, we use the detection of both the approaching and receding hotspots, as well as the published results of VLBA observations, to comment on the kinematics of the jet.

The flux ratio between the northern and southern hotspots can be used to determine the permitted values for β and θ by using equation (1.10), with the exponent being modified to $2 + \alpha$ since the hotspots are not highly relativistic (e.g., Longair & Riley 1979). We do this individually for the radio, near-IR, and X-ray bands. We used the spectral index α for each band (0.85 for radio, 1.50 for near-IR$-$optical, and 0.83 for X-ray; see Figure 4.1, lower right panel). The calculated jet/counter-jet hotspot flux ratio differs significantly between bands: $3.34 \pm .01$ in the radio, 9.03 ± 0.36 in the near-IR, and 5.34 ± 1.61 in the X-ray.

Jorstad et al. (2005) used VLBA observations and determined the most likely viewing angle to be $18^\circ.1 \pm 5^\circ.0$ on the parsec scale. Oh et al. (2015) more recently used VLBI observations to constrain the viewing angle of 3C 111 on mas scales to $\theta \lesssim 20^\circ$ and the intrinsic velocity to $\beta \gtrsim 0.98$, in agreement with the findings of Jorstad et al. (2005) (see §1.8). We found the permitted range of β and θ for the VLBA scale by using their value for the transverse apparent $\beta_{\perp,app}$ to solve equation (1.4). Figure 4.2 shows the β versus θ plot for the parsec-scale VLBA results as well as the $\sim$100 kpc-scale hotspots using our data for each band. We see a clear deceleration from $\beta \gtrsim 0.96$ at the parsec scale to $\beta \sim$ 0.2-0.4 at the hotspot, with the velocity of the radio-emitting plasma significantly slower than that of the X-ray- and near-IR-emitting plasma. This is consistent with the two-component synchrotron model due to the fact that the radio- and X-ray-emitting electron populations appear to be moving at significantly different velocities, however it may require that the near-IR-emitting electrons do not occupy the

entire jet cross-section, as in the simplest version of this scenario the near-IR and radio emission come from the same spectral component. Given the relatively modest beaming we find, it is interesting that no jet components are seen in the counter-jet between the nucleus and SHS. Given the large assumptions and the probable complex structure and dynamics of the hotspot regions, this analysis serves to place an upper limit on the amount of beaming in the jet. The analysis is inconsistent with a highly beamed jet, as we would expect the jet/counter-jet hotspot flux ratio to be larger if beaming were higher.

Future observations (discussed in §4.4) will allow us to better constrain the near-IR spectral index and elaborate on these issues. The spectral index used for the radio is based on the assumption that the slope is constant up to the near-IR. We plan to improve on this value in a future paper where we analyze in-hand EVLA observations (C, X, and Ku bands) of 3C 111. A harder spectral index for the radio would increase the likely value for β, however the offset would not be large enough to bring it into agreement with the near-IR, where the $\Delta\beta \sim 0.1$. This uncertainty does not affect the small $\Delta\beta$ between the X-ray and near-IR, though the near-IR spectral slope could change a small amount with additional *HST* bands to fit the slope.

While the viewing angle has a rather large uncertainty, the β value is much more constrained. The relative difference in β between bands is preserved no matter the viewing angle, adding to the evidence that there are two electron populations moving at significantly different speeds.

The jet to counter-jet length ratio is in relatively good agreement with the radio jet to counter-jet flux ratio. The approaching jet is ∼121 arcsec in length and the counter-jet is ∼74 arcsec in length, giving a length ratio of 1.64. For a jet moving at a constant speed β and angle θ, we can apply equation (1.12). Assuming $\theta = 18°.1$, we get a value of $\beta = 0.254$, which matches well with the findings of Figure 4.2, although this

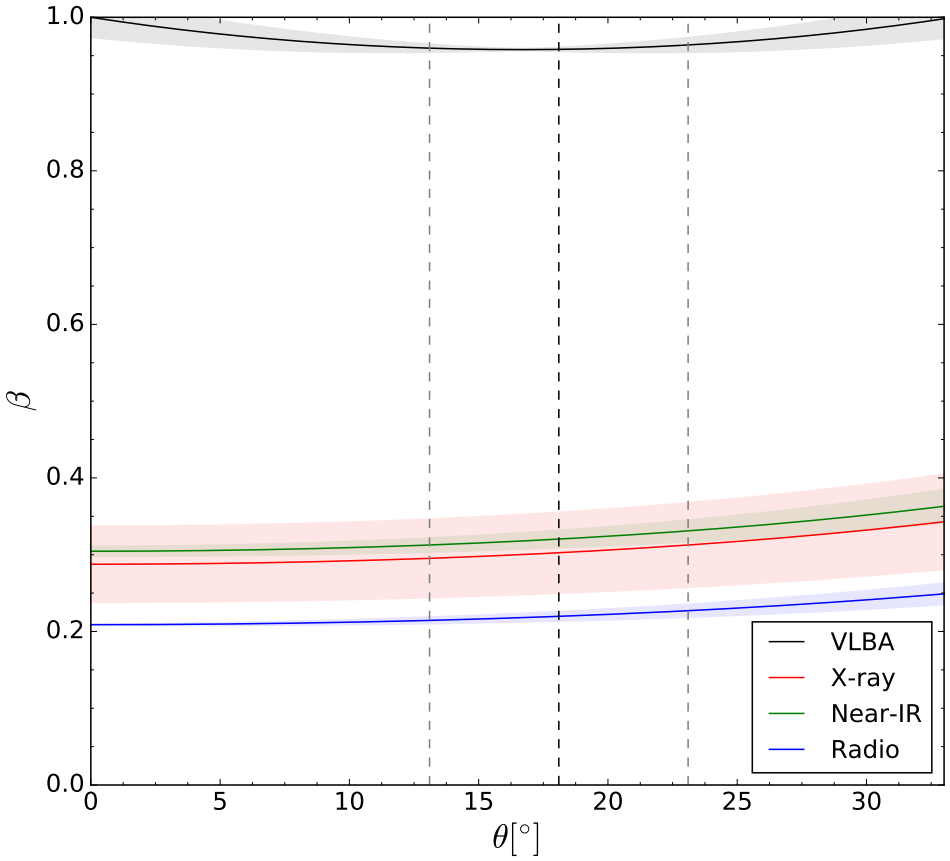

Figure 4.2 Plot of $\beta = v/c$ vs. viewing angle for the VLBA scale (solid black line) and the ∼100 kpc hotspot scale radio (blue), near-IR (green), and X-ray (red). 1σ uncertainties shown as shaded regions. The dotted lines indicate the VLBA-scale likely viewing angle of $18°.1 \pm 5°.0$.

is dependent on how the approaching and receding jets decelerate (e.g., Ryle & Longair 1967) and whether there is bending in either jet.

4.3 Modeling of the SED

The spectral indices we have obtained for K30, K61, and the NHS are all such that they must lie on either the low-energy tail or near the turnover of the second emission component. Synchrotron and EC/CMB models predict differing slopes for the emission from the very lowest energy electrons, namely $\alpha = -1/3$ for synchrotron and $\alpha = -1$ for

EC/CMB (e.g., Stawarz & Petrosian 2008; Dermer et al. 2009). If the observed spectral index at any part of the low-energy tail were to become significantly harder than $-1/3$, then that would rule out synchrotron as the dominant emission mechanism.

Figure 4.3 shows the spectral indices for various overlapping energy ranges. All three regions are in good agreement with constant spectral slopes across the entire $0.5-7.0$ keV band; none are hard enough so as to rule out synchrotron emission.

Using the parsec-scale likely viewing angle of $18°.1$ and the associated values for β from Figure 4.2 (discussed in §4.2), we can make approximations for the values of the bulk Lorentz factor Γ and the Doppler factor δ in order to model the SED for the synchrotron and EC/CMB cases for the NHS.

We used the Compton Sphere suite[1] to generate models of synchrotron and inverse-Compton emission from the K61 and NHS regions. Our observations lack enough data points to determine an accurate model, however it is sufficient to constrain model parameters. To that end, we wrote a Python wrapper to increase the usability of Compton Sphere. Inherently, Compton Sphere takes in several jet parameters (e.g., Doppler factor, comoving luminosity, $\gamma_{\rm min}$, $\gamma_{\rm max}$, magnetic field strength) and computes the associated synchrotron and EC/CMB spectra. The Python wrapper we wrote allows for a range of values for each parameter to be entered and the resulting multitude of models to be stored in an efficient HDF5 container (using the Python Data Analysis Library (pandas)). This allowed us to consider a wide range of parameters to determine the models that best fit our observations using χ^2 minimization. We hope to expand on this code in the future and allow for the calculation of many other jet diagnostics beyond the spectra, as well as utilizing Bayesian methods to best determine the model fitting.

Figure 4.4 shows several attempts at modeling the SED of K61 and the NHS with varying parameters for the synchrotron model using the Compton Sphere suite.

[1]Found at `http://astro.umbc.edu/compton`

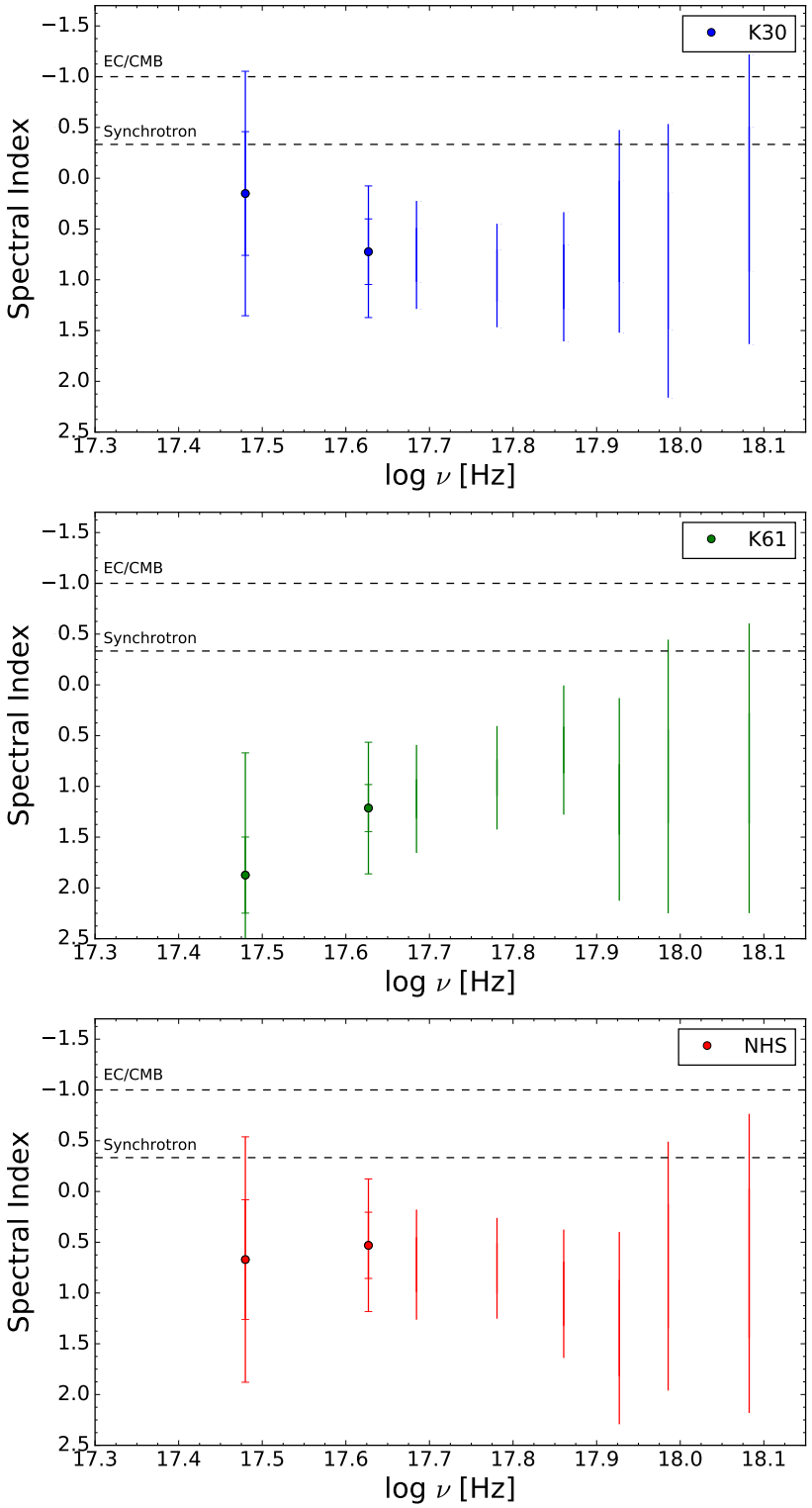

Figure 4.3 X-ray spectral indices for various overlapping energy ranges with error bars for 68% and 95% confidence intervals. Energy ranges: 0.5−2, 0.5−3, 0.5−3.5, 1−4, 1.5−4.5, 2−5, 2.5−5.5, 3−7 keV. The labeled dashed lines indicate the predicted spectral indices for the low-energy tail of the synchrotron and EC/CMB models.

In the case of K61, our near-IR and X-ray data serve to constrain the low-energy tail of the second emission component. However, because the near-IR spectrum for K61 is not available, we are not able to determine whether the detected flux is dominated by the first or second emission components − the spectrum could be either falling in the near-IR as the first synchrotron component dies off, or it could be rising as the second emission component ramps up. The future *HST* observations we have been allotted time for include two filters (in addition to F160W) that should allow us to constrain which emission component is responsible for the detected near-IR flux (see §4.4). We have plotted two example models for the second emission component showing these possibilities using a magnetic field strength ranging over $B = (1 - 3.2) \times 10^{-5}$ G, with $\gamma_{max} = (3.6 - 10) \times 10^9$, and $\gamma_{min} = (1.3 - 3.6) \times 10^7$, with a comoving luminosity of 2.15×10^{42} erg s^{-1}. The magnetic field strength B and fitted γ_{max} values translate to a radiative lifetime of ∼100 years, which is difficult to explain without distributed *in situ* acceleration − this requirement can be relaxed by using a lower value of B.

Varying several of the input parameters can have a large effect on the shape of the curve above 7 keV for K61 and especially in the case of the NHS. The bottom of Figure 4.4 shows several representative models for the SED of the NHS that go into hard X-rays (and the *NuSTAR* energy band). Unlike K61, the low-energy tail of the second emission component of the NHS is not constrained by the radio or near-IR data. The models shown here vary wildly in emission above 7 keV, where the magnetic field strengths range over $B = (0.2 - 1) \times 10^{-4}$ G, with $\gamma_{max} = (1.9 - 100) \times 10^8$, and $\gamma_{min} = (5.2 - 27) \times 10^3$, with a comoving luminosity of 1×10^{43} erg s^{-1}.

If the X-ray emission is due only to EC/CMB, then an estimate of the magnetic field strength can be made using

$$\frac{S_{sync}}{S_{IC}} = \frac{(2 \times 10^4 T)^{(3-p)/2} B_{\mu G}^{(1+p)/2}}{8\pi\rho} \tag{4.1}$$

(Felten & Morrison, 1966), where $\rho = \Gamma^2 \rho_0 (1+z)^4$ is the apparent energy density of the CMB at redshift z, $\rho_0 = 4.19 \times 10^{-13}$ erg cm^{-3} is the local CMB energy density, the apparent temperature of the CMB is δT, and the temperature of the CMB is $T = 2.728(1+z)$ K. This calculation gives a value of $B \approx 7.9 \times 10^{-5}$ G. While this is comparable to that quoted for other jets where the EC/CMB model is used to model their X-ray emission, in this case a comoving luminosity of $\sim 10^{51}$ erg s^{-1} is required to fit the model to our X-ray data. We feel this is unrealistic, as it would violate the Eddington limit by many orders of magnitude. For that reason, we have not shown it in any figure.

Additionally, assuming an equipartition magnetic field, a Doppler factor of $\delta \sim 45$ is required for EC/CMB to explain the observed X-ray/radio NHS flux even for the case of $\theta = 0°$ using standard formulae (Harris & Krawczynski, 2002). The required beaming is highly unlikely given the observed properties of the 3C 111 jet, e.g., the observed brightness of the SHS and the lack of obvious blazar properties.

We do not currently have many data points with which to constrain the model of the low-energy synchrotron component, especially in K30 and K61. We expect to be able model its SED well in follow-up work using our in-hand EVLA observations of the jet.

4.4 Future Work

Due to the promising results of this project, we were awarded with additional observations with *HST* (5 orbits in Cycle 24 + 3 orbits in Cycle 25), *Chandra* (90 ks each in Cycles 18 and 19), and the Nuclear Spectroscopic Telescope Array (*NuSTAR*) (100 ks). We also possess in-hand observations from the Karl G. Jansky Very Large Array

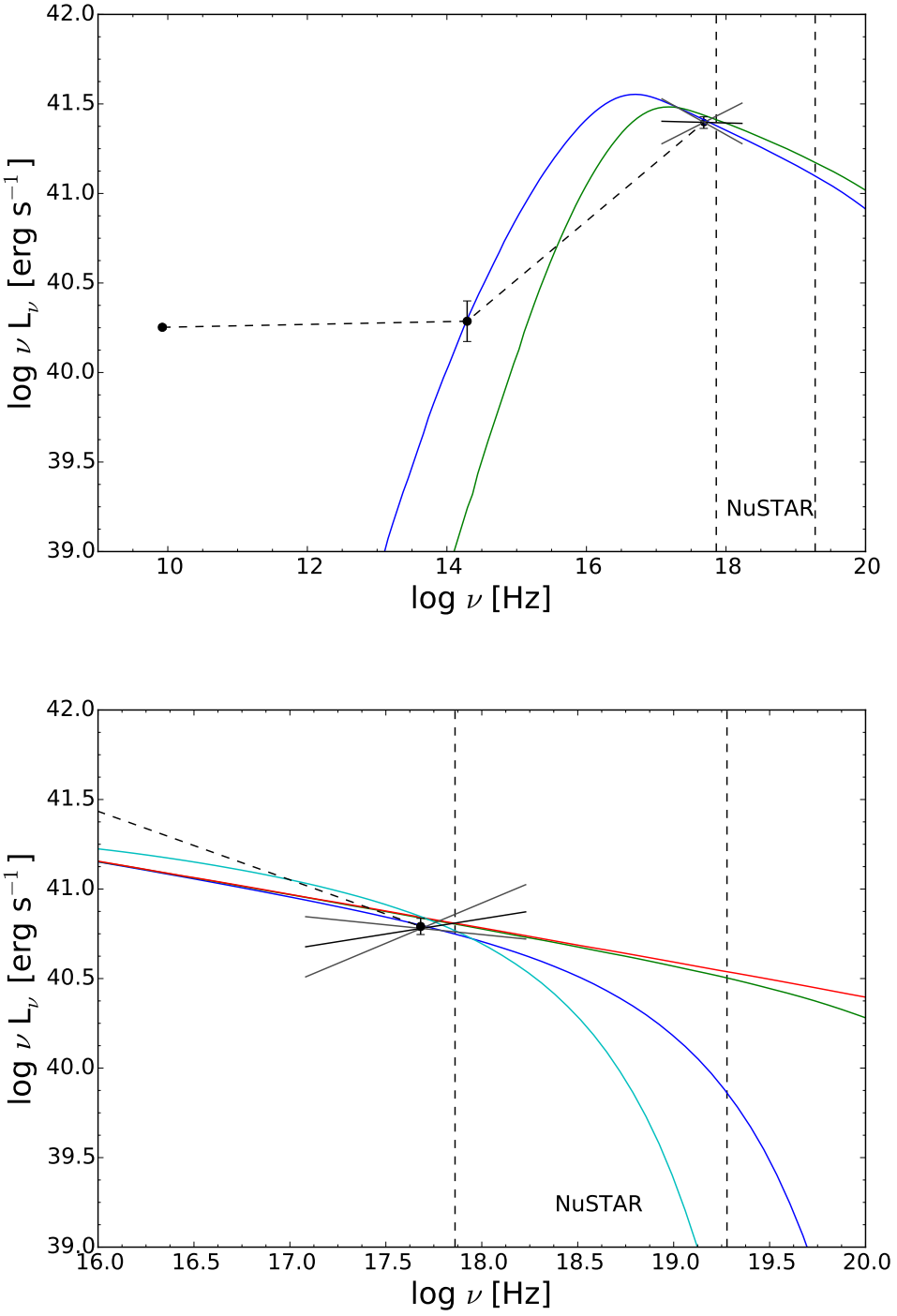

Figure 4.4 Representative models for the SED of the high-energy synchrotron component along with our binned X-ray data for K61 (*top*) and the NHS (*bottom*). Dashed vertical lines represent the boundaries of the energy range that *NuSTAR* is capable of observing.

(VLA/EVLA/JVLA) with a total time of 8 hours distributed between A and B configurations and C, X, and Ku bands. With these new observations, we will be able to improve on nearly every aspect of our current analysis, as well as areas that were not previously possible due to lack of sufficient data.

With regard to morphology, knot K61 exhibits a complex morphology in both the radio and X-ray, possessing two flux peaks in the X-ray. Our new VLA and *Chandra* observations will allow us to greatly improve on the morphological comparison in this complex emission region. Our additional *Chandra* observations will give us sufficient counts with which to compare the peak flux maxima between the X-ray and other bands. Additionally, our current *Chandra* data was sufficient for a detection of both the approaching and receding X-ray lobes (the latter is shown in Figure 4.5). Such a detection is rare, with only five cases currently known according to the XJET database[2]. Our additional observations should bring the detection of each X-ray lobe to above the 5σ level and allow us to analyze and compare the morphology and emission mechanisms of the X-ray and radio lobes.

As well, our future *HST* and *Chandra* observations will help us to better constrain the near-IR to optical and X-ray spectral indices of the jet components. The increased number of counts should also allow us to analyze the X-ray spectra and constrain the X-ray emission mechanism of fainter jet components. Both sets of observations, spaced several years apart, will allow us to test for any variability in jet emission.

Our upcoming *NusTAR* observations will allow us to constrain the SED up to $\sim$80 keV for the NHS and likely for K61 as well, allowing us to better model and distinguish between the high-energy emission mechanisms at work. 3C 111 is one of just two FR II jets that have a large enough angular size to resolve with *NuSTAR* (the other being Pictor A) 3C 111 extends two arcminutes while *NuSTAR* has a resolution of $\sim$10 arcsec.

[2] `http://hea-www.harvard.edu/XJET/`

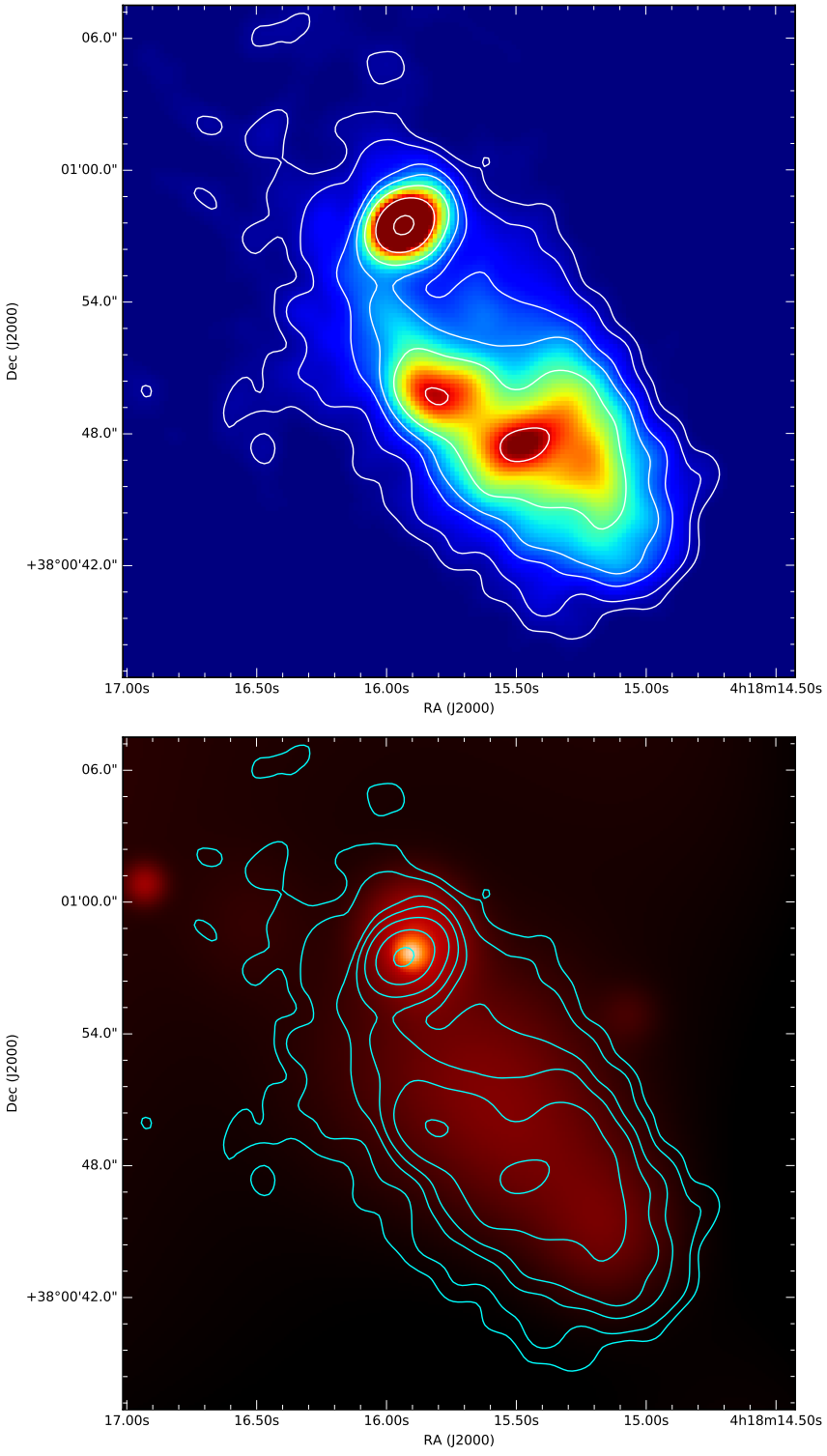

Figure 4.5 Counter-jet hotspot (SHS) and associated lobe in the archival radio (*top*) and smoothed *Chandra* (*bottom*) images, with radio contours overlaid. The X-ray lobe seems in reasonably good agreement with that of the radio and is detected at the 2.9σ level.

Chapter 5

Conclusions

We have presented new *Chandra* and *HST* observations of 3C 111 that reveal that its jet has eight X-ray and near-IR/optical emitting components, which extend for 121 arcsec (355 kpc deprojected length) from its AGN nucleus in the approaching jet, and also reveal the hotspot emission on the counter-jet side. The 3C 111 jet is remarkable for several reasons. While some other jets are comparably long, no other known jet boasts the same combination of length, number of visible components, and low redshift that 3C 111 does. For example, the jet of Pic A (Marshall et al., 2010; Gentry et al., 2015; Hardcastle et al., 2016), which is similarly straight, longer in angular extent (almost 4 arcmin), and is about 30% nearer, has only three components that have been detected in the near-IR, while the jet of 3C 273 (Jester et al., 2006), which extends for a somewhat greater distance from its host galaxy and is somewhat brighter, is nearly 4 times as far at a redshift $z = 0.158$.

The analysis discussed in this paper strongly disfavors the EC/CMB model as the dominant X-ray emission mechanism in several of the components of 3C 111's jet. The hotspot flux ratio for each of the bands we have shows the jet to have decelerated to, at most, $\beta \sim 0.4$. This, combined with a relatively high viewing angle of $\theta \sim 18°.1$

based on prior VLBA observation results, was used in our efforts to model the spectral energy distribution and showed that EC/CMB demands a power requirement many orders of magnitude above the Eddington limit for it to be the dominant X-ray emission mechanism in the jet.

We instead favor a two-component synchrotron model. Morphological comparison between radio, near-IR, and X-ray bands for K30 and the NHS show the X-ray flux maxima to be significantly upstream of the maxima in the radio, suggesting the presence of two separate electron populations with distinct energy distributions in these regions. This evidence is compounded by the analysis of the jet/counter-jet hotspot flux ratio for each band, which shows the near-IR- and X-ray-emitting electrons to be moving at a significantly faster velocity than that of the radio-emitting electron population.

Based on the results presented here, we have been awarded additional *HST*, *Chandra*, and *NuSTAR* observations of the 3C 111 jet. These data will allow us to greatly expand on the analyses conducted thus far. With them, we hope to be able to determine the near-IR and X-ray spectra of many more jet knots and pin-down the X-ray emission mechanism in the jet to a much greater degree. *NuSTAR* will let us determine the SED up to 80 keV for the approaching hotspot, and potentially for knot K61 and the receding hotspot as well. Tripling our *Chandra* exposure time will allow us to analyze the X-ray lobes, a largely unexplored area of jet physics. Our in-hand EVLA data will also enable us to fully characterize the low-energy synchrotron component in many regions of the jet.

Bibliography

Anderson, J., *Instructions for Using the Alpha-Release of the WFC3/UVIS Pixel-based CTE Correction*, Space Telescope Science Institute, Baltimore, 2013, available at `www.stsci.edu/hst/wfc3/tools/cte_tools`

Arnaud, K., Smith, R., & Siemiginowska, A., *Handbook of X-ray Astronomy*, 2011

Astropy Collaboration, Robitaille, T. P., Tollerud, E. J., et al., *Astropy: A community Python package for astronomy*, Astronomy & Astrophysics, 2013, 558, A33

Avila, R. J., Hack, W., Cara, M., et al., *DrizzlePac 2.0 - Introducing New Features*, *Astronomical Data Analysis Software an Systems XXIV (ADASS XXIV)*, (edited by A. R. Taylor & E. Rosolowsky), *Astronomical Society of the Pacific Conference Series*, vol. 495, 2015 281

Baggett, S. M., Noeske, K., Anderson, J., et al., *HST/WFC3 UVIS detectors: radiation damage effects and mitigation*, *High Energy, Optical, and Infrared Detectors for Astronomy V*, *Proc. SPIE*, vol. 8453, 2012 845336

Balbus, S. A. & Hawley, J. F., *A powerful local shear instability in weakly magnetized disks. I - Linear analysis. II - Nonlinear evolution*, The Astrophysical Journal, 1991, 376, 214–233

Biretta, J., *TinyTIM Modeling of WFC3/IR Images*, Tech. rep., 2012

Biretta, J., *Improved TinyTIM Models for WFC3/IR*, Tech. rep., 2014

Blandford, R. D. & Payne, D. G., *Hydromagnetic flows from accretion discs and the production of radio jets*, Monthly Notices of the Royal Astronomical Society, 1982, 199, 883–903

Blandford, R. D. & Znajek, R. L., *Electromagnetic extraction of energy from Kerr black holes*, Monthly Notices of the Royal Astronomical Society, 1977, 179, 433–456

Blundell, K. M. & Alexander, P., *Spectral-index asymmetries in radio galaxies: The effects of projection and light traveltime*, Monthly Notices of the Royal Astronomical Society, 1994, 267, 241–246

Boettcher, M., Harris, D. E., & Krawczynski, H., *Relativistic Jets from Active Galactic Nuclei*, 2012

Bradt, H., *Astrophysics Processes*, 2014

Brenneman, L. W. & Reynolds, C. S., *Constraining Black Hole Spin via X-Ray Spectroscopy*, The Astrophysical Journal, 2006, 652, 1028–1043

Cara, M., Perlman, E. S., Uchiyama, Y., et al., *Polarimetry and the High-energy Emission Mechanisms in Quasar Jets: The Case of PKS 1136-135*, The Astrophysical Journal, 2013, 773, 186

Cash, W., *Parameter estimation in astronomy through application of the likelihood ratio*, The Astrophysical Journal, 1979, 228, 939–947

Celotti, A., Ghisellini, G., & Chiaberge, M., *Large-scale jets in active galactic nuclei: multiwavelength mapping*, Monthly Notices of the Royal Astronomical Society, 2001, 321, L1–L5

Chandra team, *The Chandra Proposers' Observatory Guide, Version 17.0*, Chandra X-ray Center, Massachusetts, 2014, available at `cxc.harvard.edu/proposer/POG`

Chandra team, *ACIS QE Contamination*, Chandra X-ray Center, Massachusetts, 2015, available at `cxc.harvard.edu/ciao/why/acisqecontam.html`

Clautice, D., Perlman, E. S., Georganopoulos, M., et al., *The Spectacular Radio-near-IR-X-Ray Jet of 3C 111: The X-Ray Emission Mechanism and Jet Kinematics*, The Astrophysical Journal, 2016, 826, 109

Condon, J., *An Analysis of the VLASS Proposal*, ArXiv e-prints, 2015

Dermer, C. D., Finke, J. D., Krug, H., & Böttcher, M., *Gamma-Ray Studies of Blazars: Synchro-Compton Analysis of Flat Spectrum Radio Quasars*, The Astrophysical Journal, 2009, 692, 32-46

Dressel, L., *Wide Field Camera 3 Instrument Handbook, Version 7.0*, Space Telescope Science Institute, Baltimore, 2015, available at `www.stsci.edu/hst/wfc3/`

Fanaroff, B. L. & Riley, J. M., *The morphology of extragalactic radio sources of high and low luminosity*, Monthly Notices of the Royal Astronomical Society, 1974, 167, 31P–36P

Felten, J. E. & Morrison, P., *Omnidirectional Inverse Compton and Synchrotron Radiation from Cosmic Distributions of Fast Electrons and Thermal Photons*, The Astrophysical Journal, 1966, 146, 686

Freeman, P., Doe, S., & Siemiginowska, A., *Sherpa: a mission-independent data analysis application*, *Astronomical Data Analysis*, (edited by J.-L. Starck & F. D. Murtagh), *Proc. SPIE*, vol. 4477, 2001 76–87

Fruscione, A., McDowell, J. C., Allen, G. E., et al., *CIAO: Chandra's data analysis system*, *Society of Photo-Optical Instrumentation Engineers (SPIE) Conference Series*, *Proc. SPIE*, vol. 6270, 2006 62701V

Gentry, E. S., Marshall, H. L., Hardcastle, M. J., et al., *Optical Detection of the Pictor A Jet and Tidal Tail: Evidence against an IC/CMB jet*, The Astrophysical Journal, 2015, 808, 92

Giovannini, G., Taylor, G. B., Arbizzani, E., et al., *B2 1144+35: A Giant Low-Power Radio Galaxy with Superluminal Motion*, The Astrophysical Journal, 1999, 522, 101–112

Gonzaga, S., Hack, W., Fruchter, A., & Mack, J., *The DrizzlePac Handbook*, Space Telescope Science Institute, Baltimore, 2012, available at `drizzlepac.stsci.edu`

Hardcastle, M. J., Birkinshaw, M., & Worrall, D. M., *Chandra observations of the X-ray jet in 3C 66B*, Monthly Notices of the Royal Astronomical Society, 2001, 326, 1499–1507

Hardcastle, M. J., Lenc, E., Birkinshaw, M., et al., *Deep Chandra observations of Pictor A*, Monthly Notices of the Royal Astronomical Society, 2016, 455, 3526–3545

Harris, D. E. & Krawczynski, H., *X-Ray Emission Processes in Radio Jets*, The Astrophysical Journal, 2002, 565, 244–255

Harris, D. E. & Krawczynski, H., *X-Ray Emission from Extragalactic Jets*, Annual Review of Astronomy & Astrophysics, 2006, 44, 463–506

Harris, D. E. & Krawczynski, H., *Constraints on the Nature of Jets from KPC Scale X-Ray Data*, *Revista Mexicana de Astronomia y Astrofisica, vol. 27*, *Revista Mexicana de Astronomia y Astrofisica, vol. 27*, vol. 27, 2007 188

Hogan, B. S., Lister, M. L., Kharb, P., et al., *Chandra Discovery of 10 New X-ray Jets Associated with FR II Radio Core-selected AGNs in the MOJAVE Sample*, The Astrophysical Journal, 2011, 730, 92

Howell, S. B., *Two-dimensional aperture photometry - Signal-to-noise ratio of point-source observations and optimal data-extraction techniques*, Publications of the Society of the Pacific, 1989, 101, 616–622

Howell, S. B., *Handbook of CCD Astronomy*, 2006

Howell, S. B., Koehn, B., Bowell, E., & Hoffman, M., *Detection and Measurement of Poorly Sampled Point Sources Imaged With 2-D Array*, The Astronomical Journal, 1996, 112, 1302

Jester, S., Harris, D. E., Marshall, H. L., & Meisenheimer, K., *New Chandra Observations of the Jet in 3C 273. I. Softer X-Ray than Radio Spectra and the X-Ray Emission Mechanism*, The Astrophysical Journal, 2006, 648, 900–909

Jiang, L., Fan, X., Ivezić, Ž., et al., *The Radio-Loud Fraction of Quasars is a Strong Function of Redshift and Optical Luminosity*, The Astrophysical Journal, 2007, 656, 680–690

Jorstad, S. G., Marscher, A. P., Lister, M. L., et al., *Polarimetric Observations of 15 Active Galactic Nuclei at High Frequencies: Jet Kinematics from Bimonthly Monitoring with the Very Long Baseline Array*, The Astronomical Journal, 2005, 130, 1418–1465

Kellermann, K. I., Sramek, R., Schmidt, M., et al., *VLA observations of objects in the Palomar Bright Quasar Survey*, The Astronomical Journal, 1989, 98, 1195–1207

Konar, C., Jamrozy, M., Saikia, D. J., & Machalski, J., *A multifrequency study of giant radio sources - I. Low-frequency Giant Metrewave Radio Telescope observations of selected sources*, Monthly Notices of the Royal Astronomical Society, 2008, 383, 525–538

Krichbaum, T. P., Graham, D. A., Bremer, M., et al., *Sub-Milliarcsecond Imaging of Sgr A* and M 87*, Journal of Physics Conference Series, 2006, 54, 328–334

Krist, J. E., Hook, R. N., & Stoehr, F., *20 years of Hubble Space Telescope optical modeling using Tiny Tim*, *Optical Modeling and Performance Predictions V*, *Proc. SPIE*, vol. 8127, 2011 81270J

Lauer, T. R., Ajhar, E. A., Byun, Y.-I., et al., *The Centers of Early-Type Galaxies with HST.I.An Observational Survey*, The Astronomical Journal, 1995, 110, 2622

Leahy, J. P., Black, A. R. S., Dennett-Thorpe, J., et al., *A study of FRII radio galaxies with z<0.15 - II. High-resolution maps of 11 sources at 3.6 CM*, Monthly Notices of the Royal Astronomical Society, 1997, 291, 20–53

Li, J., Kastner, J. H., Prigozhin, G. Y., et al., *Chandra ACIS Subpixel Event Repositioning: Further Refinements and Comparison between Backside- and Frontside-illuminated X-Ray CCDs*, The Astrophysical Journal, 2004, 610, 1204–1212

Lister, M. L., Cohen, M. H., Homan, D. C., et al., *MOJAVE: Monitoring of Jets in Active Galactic Nuclei with VLBA Experiments. VI. Kinematics Analysis of a Complete Sample of Blazar Jets*, The Astronomical Journal, 2009, 138, 1874-1892

Lister, M. L. & Marscher, A. P., *Statistical Effects of Doppler Beaming and Malmquist Bias on Flux-limited Samples of Compact Radio Sources*, The Astrophysical Journal, 1997, 476, 572–588

Liu, W.-P., *An IC/CMB interpretation for the large-scale jet X-ray emission of 3C 273*, ArXiv e-prints, 2015

Longair, M. S. & Riley, J. M., *Statistical evidence on the dynamical evolution of extended radio sources*, Monthly Notices of the Royal Astronomical Society, 1979, 188, 625–635

Marshall, H. L., Hardcastle, M. J., Birkinshaw, M., et al., *A Flare in the Jet of Pictor A*, Astrophysical Journal Letters, 2010, 714, L213–L216

McMaster, M. et al., *Wide Field and Planetary Camera 2 Instrument Handbook v. 10.0*, 2008

McMullin, J. P., Waters, B., Schiebel, D., et al., *CASA Architecture and Applications*, *Astronomical Data Analysis Software and Systems XVI*, (edited by R. A. Shaw, F. Hill, & D. J. Bell), *Astronomical Society of the Pacific Conference Series*, vol. 376, 2007 127

Mehta, K. T., Georganopoulos, M., Perlman, E. S., et al., *Hubble Space Telescope Observations of the Quasar PKS 0637-752: Equipartition Electron-Proton Jet from the Most Complete Spectral Coverage to Date*, The Astrophysical Journal, 2009, 690, 1706–1714

Meier, D. L., *A Magnetically Switched, Rotating Black Hole Model for the Production of Extragalactic Radio Jets and the Fanaroff and Riley Class Division*, The Astrophysical Journal, 1999, 522, 753–766

Meier, D. L., *The formation of relativistic cosmic jets*, *Jets at All Scales*, (edited by G. E. Romero, R. A. Sunyaev, & T. Belloni), *IAU Symposium*, vol. 275, 2011 13–23

Meisenheimer, K., Roser, H.-J., Hiltner, P. R., et al., *The synchrotron spectra of radio hot spots*, Astronomy & Astrophysics, 1989, 219, 63–86

Meisenheimer, K., Yates, M. G., & Roeser, H.-J., *The synchrotron spectra of radio hot spots. II. Infrared imaging.*, Astronomy & Astrophysics, 1997, 325, 57–73

Meyer, E. T. & Georganopoulos, M., *Fermi Rules Out the Inverse Compton/CMB Model for the Large-scale Jet X-Ray Emission of 3C 273*, Astrophysical Journal Letters, 2014, 780, L27

Meyer, E. T., Georganopoulos, M., Sparks, W. B., et al., *Ruling out IC/CMB X-rays in PKS 0637-752 and the Implications for TeV Emission from Large-scale Quasar Jets*, The Astrophysical Journal, 2015, 805, 154

Moderski, R., Sikora, M., & Lasota, J.-P., *On the spin paradigm and the radio dichotomy of quasars*, Monthly Notices of the Royal Astronomical Society, 1998, 301, 142–148

Nyquist, H., *Certain Topics in Telegraph Transmission Theory*, Transactions of the American Institute of Electrical Engineers, Volume 47, Issue 2, pp. 617-624, 1928, 47, 617–624

Oh, J., Trippe, S., Kang, S., et al., *PAGaN II: The Evolution of AGN Jets on Sub-Parsec Scales*, Journal of Korean Astronomical Society, 2015, 48, 299–311

Perlman, E. S. & Wilson, A. S., *The X-Ray Emissions from the M87 Jet: Diagnostics and Physical Interpretation*, The Astrophysical Journal, 2005, 627, 140–155

Perucho, M. & Martí, J. M., *A numerical simulation of the evolution and fate of a Fanaroff-Riley type I jet. The case of 3C 31*, Monthly Notices of the Royal Astronomical Society, 2007, 382, 526–542

Peterson, B. M., *An Introduction to Active Galactic Nuclei*, 1997

Rajan, A. et al., *WFC3 Data Handbook, Version 2.1*, Space Telescope Science Institute, Baltimore, 2010, available at `www.stsci.edu/hst/wfc3/`

Rees, M. J., *Appearance of Relativistically Expanding Radio Sources*, Nature, 1966, 211, 468–470

Roeser, H.-J., Conway, R. G., & Meisenheimer, K., *The synchrotron radiation from the jet of 3C273. IV. Comparison of optical and radio morphology and polarization.*, Astronomy & Astrophysics, 1996, 314, 414–418

Rots, A. H. & Budavári, T., *Determining the Absolute Astrometric Error in Chandra Source Catalog Positions*, The Astrophysical Journal, Supplement, 2011, 192, 8

Rybicki, G. B. & Lightman, A. P., *Radiative processes in astrophysics*, 1979

Ryle, M., Sir & Longair, M. S., *A possible method for investigating the evolution of radio galaxies*, Monthly Notices of the Royal Astronomical Society, 1967, 136, 123

Sargent, W. L. W., *Redshifts for six 3CR radio galaxies and the spectrum of 3C 111*, Astrophysical Journal Letters, 1977, 212, L105

Schneider, P., *Extragalactic Astronomy and Cosmology*, 2006

Schwartz, D. A., Marshall, H. L., Lovell, J. E. J., et al., *Chandra Discovery of a 100 kiloparsec X-Ray Jet in PKS 0637-752*, Astrophysical Journal Letters, 2000, 540, L69

Shakura, N. I. & Sunyaev, R. A., *Black holes in binary systems. Observational appearance.*, Astronomy & Astrophysics, 1973, 24, 337–355

Sironi, L., Petropoulou, M., & Giannios, D., *Relativistic jets shine through shocks or magnetic reconnection?*, Monthly Notices of the Royal Astronomical Society, 2015, 450, 183–191

Stawarz, Ł. & Petrosian, V., *On the Momentum Diffusion of Radiating Ultrarelativistic Electrons in a Turbulent Magnetic Field*, The Astrophysical Journal, 2008, 681, 1725-1744

Tavecchio, F., Maraschi, L., Sambruna, R. M., & Urry, C. M., *The X-Ray Jet of PKS 0637-752: Inverse Compton Radiation from the Cosmic Microwave Background?*, Astrophysical Journal Letters, 2000, 544, L23–L26

Taylor, G. B., Vermeulen, R. C., Readhead, A. C. S., et al., *A Complete Flux-Density–limited VLBI Survey of 293 Flat-Spectrum Radio Sources*, The Astrophysical Journal, Supplement, 1996, 107, 37

Tchekhovskoy, A. & Bromberg, O., *Three-dimensional relativistic MHD simulations of active galactic nuclei jets: magnetic kink instability and Fanaroff-Riley dichotomy*, Monthly Notices of the Royal Astronomical Society, 2016, 461, L46–L50

Tout, C. A. & Pringle, J. E., *Can a disc dynamo generate large-scale magnetic fields?*, Monthly Notices of the Royal Astronomical Society, 1996, 281, 219–225

van Dokkum, P. G., *Cosmic-Ray Rejection by Laplacian Edge Detection*, Publications of the Society of the Pacific, 2001, 113, 1420–1427

Vikhlinin, A., *Reducing ACIS Quiescent Background Using Very Faint Mode*, Chandra X-ray Center, Massachusetts, 2002, available at `cxc.harvard.edu/cal/Acis/Cal_prods/vfbkgrnd/index.html`

Wang, J., Fabbiano, G., Risaliti, G., et al., *A Deep Chandra ACIS Study of NGC 4151. I. The X-ray Morphology of the 3 kpc Diameter Circum-nuclear Region and Relation to the Cold Interstellar Medium*, The Astrophysical Journal, 2011, 729, 75

Weisskopf, M. C., Aldcroft, T. L., Bautz, M., et al., *An Overview of the Performance of the Chandra X-ray Observatory*, Experimental Astronomy, 2003, 16, 1–68

Wilson, A. S. & Colbert, E. J. M., *The difference between radio-loud and radio-quiet active galaxies*, The Astrophysical Journal, 1995, 438, 62–71

Xie, W., Lei, W.-H., Zou, Y.-C., et al., *A two-component jet model based on the Blandford-Znajek and Blandford-Payne processes*, Research in Astronomy and Astrophysics, 2012, 12, 817–828

Zweibel, E. G. & Yamada, M., *Magnetic Reconnection in Astrophysical and Laboratory Plasmas*, Annual Review of Astronomy & Astrophysics, 2009, 47, 291–332